JOURNAL OF GEOPHYSICAL RESEARCH, VOL. 115, E00D14, doi:10.1029/2009JE003338, 2010

Spectrally distinct ejecta in Syrtis Major, Mars: Evidence for environmental change at the Hesperian-Amazonian boundary

John R. Skok,[1] John F. Mustard,[1] Scott L. Murchie,[2] Michael B. Wyatt,[1] and Bethany L. Ehlmann[1]

Received 23 January 2009; revised 30 July 2009; accepted 23 September 2009; published 27 February 2010.

[1] Analysis of visible and near-infrared (VNIR) imaging spectrometer data of the Syrtis Major volcanic complex on Mars shows spectrally distinct ejecta (SDE) around a subset of the region's impact craters. We explore the nature of this spectral difference with the intention of constraining the physical cause of the distinction and the significance of their near random spatial distribution. Crater counting performed by Baratoux et al. (2007) indicated that the craters with SDE are systematically younger than craters without SDE. Extensive crater counts of the craters with SDE show that they fit a consistent Hartmann (2005) isochron indicting that they represent temporally continuous population. This population was dated near 2 Ga, consistent with the counts of Baratoux et al. (2007). This modeled age corresponds to just after the Hesperian-Amazonian boundary, indicating that it may be related to a global event. We explore possible explanations for the lack of SDE around older craters, including atmospheric changes, significant but brief regional emplacement of materials, and volcanic activity. We conclude that the preferred explanation is that the SDE represent the true composition of the Syrtis Major volcanics and that surfaces older than 2 Ga were altered by interactions with water vapor or volcanic gases under different Hesperian climatic and atmospheric conditions leading to all craters formed after this alteration event to display SDE.

Citation: Skok, J. R., J. F. Mustard, S. L. Murchie, M. B. Wyatt, and B. L. Ehlmann (2010), Spectrally distinct ejecta in Syrtis Major, Mars: Evidence for environmental change at the Hesperian-Amazonian boundary, *J. Geophys. Res.*, *115*, E00D14, doi:10.1029/2009JE003338.

1. Introduction

[2] Syrtis Major is a broad 1100 km wide Hesperian-aged volcanic complex with an estimated flow thickness of 0.5–1 km [*Schaber et al.*, 1981; *Hiesinger and Head*, 2004]. Compositional studies of Syrtis Major using the near-infrared Imaging Spectrometer for Mars (ISM) instrument [*Bibring et al.*, 1989] documented the presence of both low-calcium pyroxenes (LCP) and high-calcium pyroxenes (HCP) in the dust-free regions [*Mustard and Sunshine*, 1995]. The lavas were interpreted to be two pyroxene-bearing basalts analogous in mineralogy to the Martian basaltic meteorites [*Mustard et al.*, 1997]. Data from the Thermal Emission Spectrometer (TES) [*Christensen et al.*, 1992] instrument yielded a regional modal mineralogy of 31% plagioclase, 29% HCP, 12% high-silica phases, 7% olivine, 4% LCP, and 17% other minerals for the low-albedo regions of Syrtis Major (Figure 1, left) [*Rogers and Christensen*, 2007]. Modal mineralogy of a similar area derived from near-infrared OMEGA data include 34% HCP, 9% LCP, 48% plagioclase, <5% olivine, and 8% other (Figure 1, right) [*Poulet et al.*, 2009a]. The results are broadly similar for Fe-bearing mafic minerals but differ for the other constituents due to varying sensitivities of the corresponding wavelength region.

[3] Reflectance spectra of pyroxene show two electronic transition absorptions near 1 and 2 μm, the exact wavelengths of which vary with cation composition [*Burns*, 1970; *Adams*, 1974; *Cloutis and Gaffey*, 1991; *Klima*, 2008]. This variation allows the use of VNIR spectroscopic data to determine the relative abundances of the HCP and LCP mineral end-members using the normalized ratio of LCP/(LCP+HCP) band strength ratio [*Kanner et al.*, 2007]. In this ratio, 1.0 indicates that all the pyroxene is LCP, and 0.0 indicates that all the pyroxene is HCP. Noachian terrain in the Nili Fossae region has an average value near 0.6, while Syrtis Major has an average value near 0.4, with more extreme values, <0.1, occurring at local scales [*Kanner et al.*, 2007]. Thus, VNIR data show that the Hesperian-aged Syrtis Major has pyroxene that are more HCP-rich than adjacent Noachian-aged terrains.

[4] Imaging spectroscopy analyses showed the presence of numerous craters across Syrtis Major with spectrally

[1]Department of Geological Sciences, Brown University, Providence, Rhode Island, USA.
[2]John Hopkins University Applied Physics Laboratory, Laurel, Maryland, USA.

0148-0227/10/2009JE003338$09.00

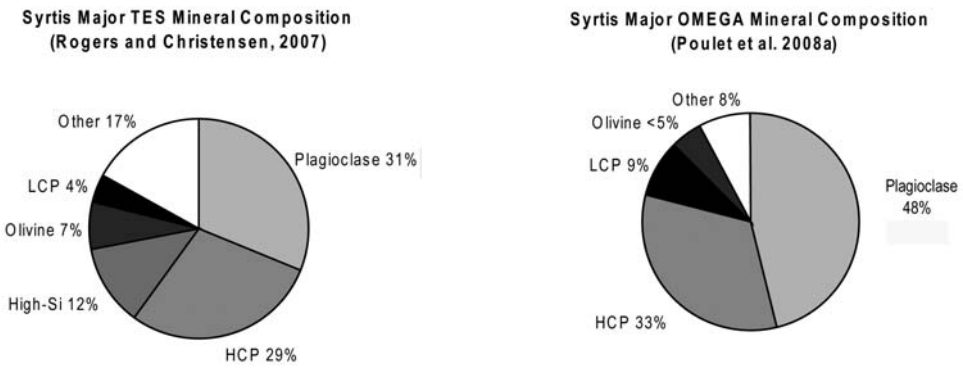

Figure 1. Composition of Syrtis Major as determined by the TES instrument with thermal infrared observations and the OMEGA instrument with near-infrared observations.

distinct ejecta blankets [*Baratoux et al.*, 2007]. These were classified as "type 1" craters whose ejecta are enriched in the HCP component of the pyroxene compared to the surrounding terrain (what we refer to as craters with SDE) and "type 2," those whose ejecta is identical in normalized pyroxene ratio to the background (non-SDE) terrain. These type classifications do not refer to the TES type 1 and 2 regions and are only used in the *Baratoux et al.* [2007] paper to distinguish between these crater types. We thus prefer the terms craters with SDE and non-SDE to distinguish the two crater types. With OMEGA data, craters with SDE do not show a distinct geographic distribution or size range with occurrences at all observable spatial scales, although there is a higher density on in the eastern side of Syrtis Major that correlates with a higher density of total crater population caused by the slighter older and better exposed surfaces in the east [*Hiesinger and Head*, 2004]. Using crater counts on the ejecta of eight of the largest Syrtis Major craters (5 type 1 (SDE), 3 type 2 (non-SDE)), *Baratoux et al.* [2007] found that the spectrally distinct type 1 (SDE) craters are younger than the nondistinct type 2 (non-SDE) craters, with a division between the types occurring near a model age of 2 Ga, according to the *Hartmann* [2005] isochrons, which are used throughout this study. The *Baratoux et al.* [2007] transition age of ~2 Ga was determined by crater counting with THEMIS-VIS imagery (~18 m per pixel) on the ejecta blankets of eight of the largest craters on Syrtis Major and noting which have SDE. Their findings suggest that the craters with SDE are systematically younger than the craters without SDE. They also showed that the diameter of HCP enrichment does not vary across the Syrtis Major complex, implying a uniform source layer.

[5] In this paper we examine the character and nature of these unusual craters, with high-resolution spectral data. We expand on aspects of *Baratoux et al.* [2007] identification and initial analysis of Syrtis Major craters with SDE using CRISM multispectral observations (200 m/pixel) to increase the spatial resolution and number of identifiable craters. We have examined the presence of SDE around small craters to determine if the craters are excavating a shallow source layer. The statistical dating methods for determining the timing of the transition between craters with SDE and those without are improved by the more extensive crater counts using the actual populations of craters with SDE. After establishing this transition date, we consider hypotheses including physical mixing processes, the excavation of underlying materials with a distinct composition, and the formation of rinds or coatings through surface-atmosphere interactions, hydration, or volcanism, both at the global and local scale.

2. Methods

2.1. Data

[6] We concentrate our investigation on the Syrtis Major volcanic terrain located from 2°S to 20°N and 60°E to 75°E (Figure 2). This regional subset was selected because it covers the majority of Syrtis Major lava flows and craters with SDE and is well covered by OMEGA observations. Our crater counts are restricted to the Syrtis Major volcanic edifice within this region.

[7] We use VNIR data from the OMEGA and CRISM instruments to produce maps of pyroxene calcium content in the Syrtis Major region. The OMEGA imaging spectrometer has a spatial resolution that varies from 5 km to 300 m per pixel and a spectral range from 0.35 μm to 5 μm spread over 352 spectral bands, each with a width of 0.014 μm [*Bibring et al.*, 2005]. The OMEGA observations were calibrated for known instrument artifacts and for atmospheric gases [*Bibring et al.*, 2005; *Bellucci et al.*, 2006]. Correction for atmospheric gases assumes that the surface and atmosphere contributions are multiplicative and that absorptions by atmospheric gases follow a power law variation with altitude [*Bibring et al.*, 1989]. The ratio between observations of the Olympus Mons summit and observations on the volcano's lower flank allows an atmospheric absorption spectrum to be derived [*Langevin et al.*, 2005]. This is scaled to each pixel in an OMEGA observation using a power law relationship from the data set to remove atmospheric contributions due to gases.

[8] The CRISM instrument has a spectral range from 0.362 μm to 3.92 μm and is capable of making targeted observations at 544 wavelengths with 6.55 nm/band spectral sampling and a spatial resolution of ~18 m/pixel and multispectral (MSP) observations over a similar wavelength range with 72 wavelength channels and a spatial resolution of ~200 m/pixel [*Murchie et al.*, 2007]. CRISM data is calibrated to radiance and divided by the solar spectrum, giving I/F values and corrected for the incidence angle. Atmospheric gas band removal is based on an atmospheric transmission spectrum derived over Olympus Mons [*Mustard et al.*,

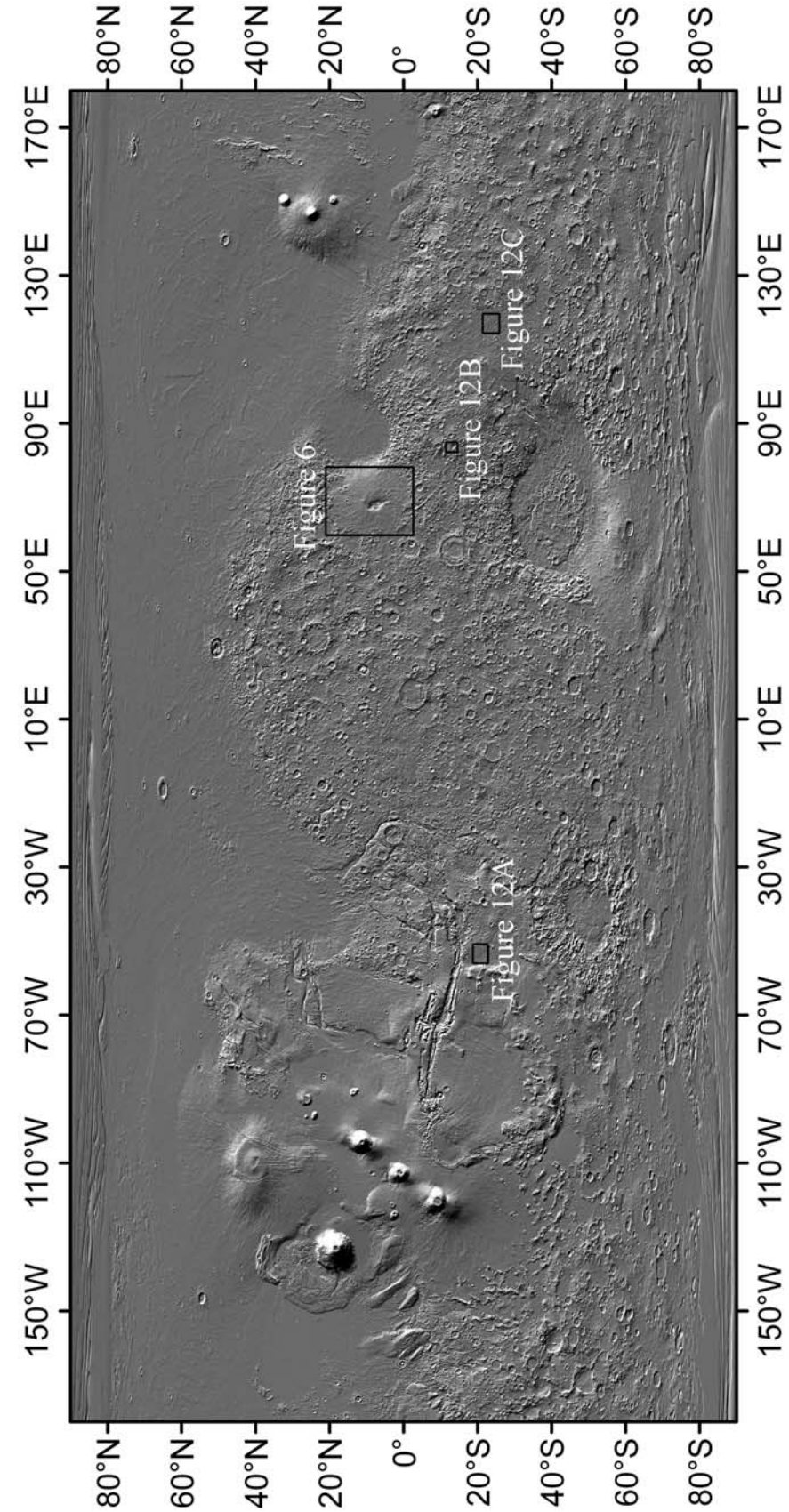

Figure 2. MOLA shaded relief map of Mars. The box corresponding to Figure 6 indicates Syrtis Major, the region of study. We have performed crater counts on Syrtis Major volcanic units that lie from 20°N to 2°S and 60°E to 75°E. Also shown is regions featured in Figure 12.

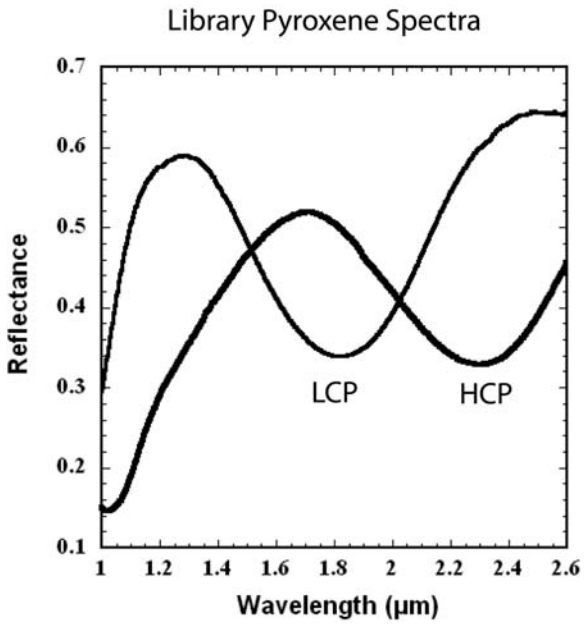

Figure 3. End-member pyroxene library spectra. HCP is a Clinopyroxene/Diopside and this spectra has absorptions near 1.05 μm and 2.3 μm; LCP is Orthopyroxene/Enstatite and has absorptions at 0.9 μm and 1.85 μm. Spectra are taken from Keck/NASA Reflectance Experiment Laboratory (RELAB)'s spectral library.

2008], similar to the method used for OMEGA atmospheric removal.

2.2. Pyroxene Spectroscopy and Modeling

[9] Pyroxene, (Ca, Fe, Mg)Si_2O_6, has an inosilicate structure that accommodates cations in tetrahedral or octahedral coordination. There are two octahedral sites (M1, M2) that can accommodate the cations Fe, Mg, and Ca. Electronic transition absorptions associated with Fe^{2+} in the M2 site produce strong broad absorptions near 1 and 2 μm, where the exact position is a function of the cation occupancy in the M1 and M2 sites. The relationship between mineral chemistry and the character of the absorption bands in pyroxene is most strongly controlled by the presence of the Ca^{2+} cation [*Burns*, 1970; *Adams*, 1974; *Cloutis and Gaffey*, 1991; *Klima*, 2008]. Low-Ca pyroxenes (LCP) such as enstatite or pigeonite typically have absorptions near 0.92 and 1.8 μm, while high-Ca pyroxenes (HCP) such as augite and diospide have absorptions near 1.02 and 2.35 μm (Figure 3). This broad separation in band position permits LCP and HCP to be readily distinguished with reflectance spectroscopy.

[10] There are several analytical methods available to determine the pyroxene content from reflectance spectroscopy. Empirical methods are based on absorption band centers and the area of the absorptions [*Cloutis and Gaffey*, 1991]. These methods are either too qualitative or do not allow for the deconvolution of mixtures. Another method, spectral mixture modeling, provides for a quantitative way to model modal mineralogy [*Mustard and Pieters*, 1989; *Poulet and Erard*, 2004]. However, due to limitations concerning the knowledge of absolute reflectance with the current CRISM calibration, a reliable unmixing algorithm has not yet been developed to the capacity needed for this study. The method that we utilize here is the Modified Gaussian Model (MGM) [*Sunshine et al.*, 1990; *Sunshine and Pieters*, 1993]. The version we use was specifically designed to decompose spectral mixtures of pyroxene to determine the relative abundance of LCP and HCP and has been modified to be suitable for use with OMEGA and CRISM data [*Gendrin*, 2004].

[11] The MGM models a spectrum's absorption features with Gaussian distributions and relates them to known absorption features. Gaussians are defined as

$$g(x) = s \cdot \exp\left(\frac{-(x-\mu)^2}{2\sigma^2}\right) \quad (1)$$

where s is band strength, σ is the band width, and μ is the band center. The MGM superimposes several Gaussians onto a continuum to model the spectrum with known absorption features at fixed wavelengths due to specific electronics transitions. This method has the power to resolve overlapping and superimposed absorption features. Typically, when the MGM is applied to pyroxene spectra, it models both the 1 and 2 μm absorption bands. However, a detector change near 1 μm in the CRISM instrument [*Murchie et al.*, 2007] limits the wavelength range for analysis to 1.0–2.6 μm. Furthermore, *Kanner et al.* [2007] showed that the 1 μm region is frequently affected by Fe crystal field absorptions of olivine, ferric oxides, and other minerals that lead to an inaccurate pyroxene result. Thus, we limit the mineralogical analysis to the modeled fit of the 2 μm pyroxene absorption band and include the 1 μm absorption to improve the model fit of pyroxene and not to determine mineralogy from this absorption's properties. We refer to the MGM that only considers the 1.0 to 2.6 μm wavelength region and models with the three absorptions described as the CRISM-specific MGM.

[12] The CRISM and OMEGA spectra are modeled as three Gaussian absorptions (Table 1) applied to a spectral continuum (Figure 4), where the initial values of each are carefully selected based on the work of *Mustard et al.* [1997]. The strengths of these absorptions and the continuum are allowed to vary, while the band centers and widths are fixed. The iterative algorithm modifies the modeled spectra until the root mean square (RMS) error of the fit is below a tolerance of 10^{-5}. If not acquired within 10 iterations the MGM fails to produce a result, otherwise the strengths of the broad 1.9 and 2.3 μm absorptions, representing LCP and HCP, respectively, are recorded as pixel values in a derived data map.

[13] *Kanner et al.* [2007] verified the use of the MGM on pyroxene mixtures and applied the method to remote sensing observations from the OMEGA instrument. They showed

Table 1. MGM Modeling End-Member Parameters[a]

	1 μm Fit	LCP End-Member	HCP End-Member
Band center (μ)	0.95 μm	1.9 μm	2.3 μm
Band width (σ)	0.4 μm	0.5 μm	0.56 μm
Band strength (s)	0.08	0.08	0.08

[a]Initial parameters for the MGM routine. The band center and width are fixed and the 2 μm Band strength is allowed to vary to fit the absorption.

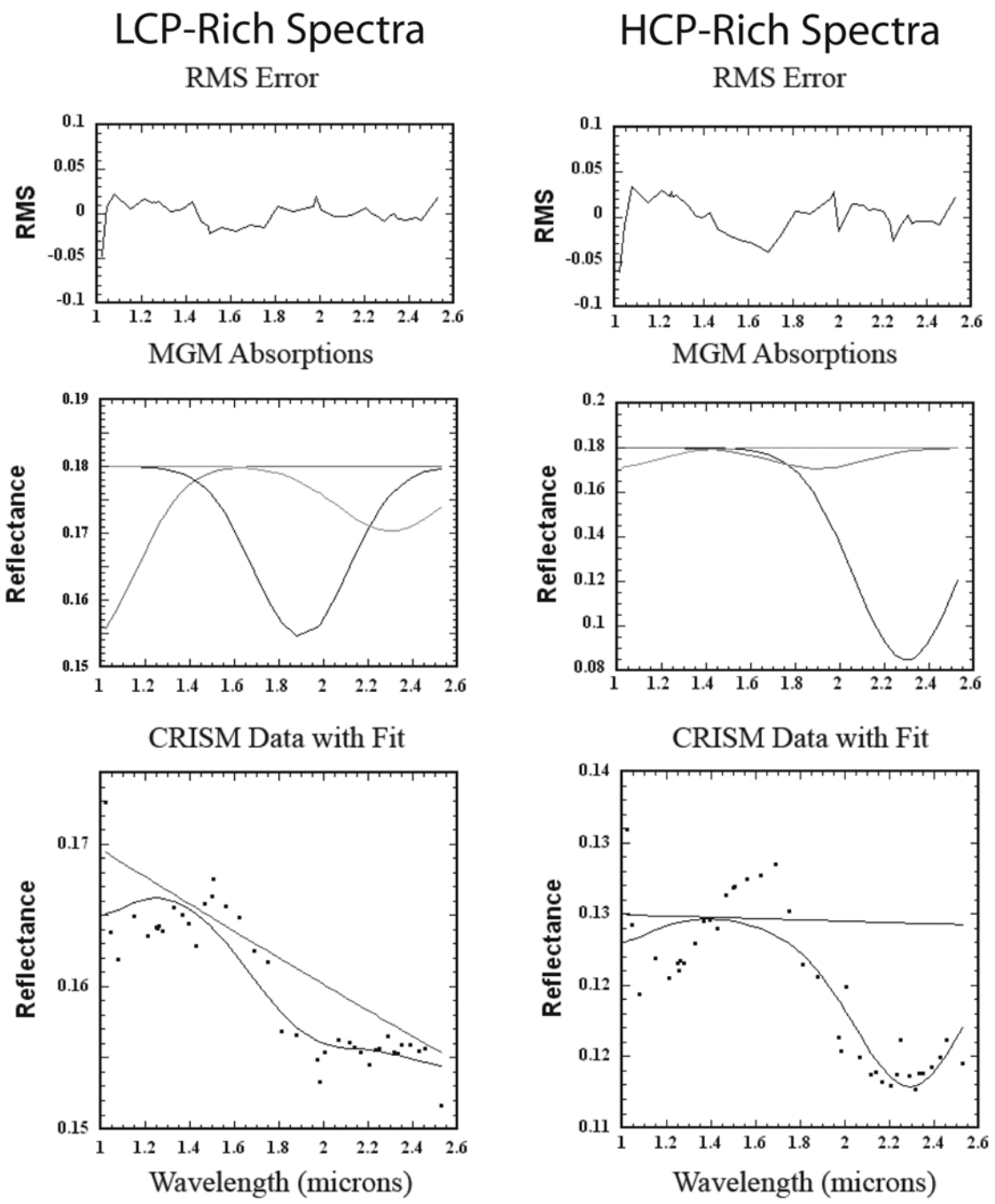

Figure 4. MGM fit of CRISM spectra taken from a 5 × 5 pixel average. HCP-rich sample centered at X:25 Y:384 of MSP00004845_03. LCP-rich sample centered at X:40 Y:833 of MSP000040BA_01. (top) RMS error, CRISM value minus modeled value. (middle) Modeled strength of Gaussian absorptions. (bottom) CRISM spectral data (dots), modeled fit (black curved line), and continuum used for modeling (straight black line). Bottom box displays the MGM result with the respective band depths for HCP, LCP, and the relative abundance ratio.

that with laboratory spectra of pyroxene mixtures, the modified MGM can determine the relative pyroxene abundances to within ±10%. These results provide a convenient and reliable way of determining the relative pyroxene abundances throughout Mars and are systematically mapped to the surface; however the current method does fail when olivine has a significant effect on the mixture's spectrum.

2.3. TES and THEMIS Data

[14] Observations from the Thermal Emission Spectrometer (TES) instrument [*Christensen et al.*, 1992] were used as an independent analyses of the compositional results from the CRISM and OMEGA VNIR instruments. TES thermal infrared (TIR) spectra were constrained by surface temperatures >250 K, lambert albedo <0.15, dust extinctions of <0.18 (1075 cm 1 opacity of ~0.3), water ice extinctions of <0.1 (800 cm 1 opacity of ~0.15), and emission angles of <30° [*Bandfield et al.*, 2000] We acquired individual TES spectra with spatial resolution of ~3 × 6 km, in areas of SDE and neighboring areas without SDE in the same spacecraft orbit. The instrument resolution limits us to only the largest craters with SDE. When possible, a 3 × 3 pixel average was used to reduce signal noise, in all cases at least seven TES pixels were averaged for a particular location.

[15] Thermalphysical properties of specific crater were also assessed using imaging data from the Thermal Emission Imaging System (THEMIS) instrument [*Christensen et al.*, 2004]. THEMIS operates both a TIR multispectral mode with nine bands between from 6.8 to 14.9 μm with 100 m per pixel resolution and a visible mode with five bands and 18 m per pixel resolution. We primarily use THEMIS night IR images where temperature variations are related to differences in the surface's physical properties. To first order, loosely consolidated materials such as dust and soil quickly lose solar heat during the night, while competent bedrock exposures retain heat longer and appear relatively bright in the night IR images. We use this property to assess craters by assuming that young, fresh craters have more exposed bedrock around their rims and appear bright in the night IR images while older craters are more filled and modified with dust and sand covering the bedrock and appear cooler [*Christensen et al.*, 2004].

[16] In order to quantify the thermal properties of Syrtis Major craters, we calculated the nighttime temperature of craters with and without SDE and compared them to the intercrater background material. Nighttime temperatures were determined from the Brightness Temperature Record (BTR) THEMIS products available on the THEMIS data Web site (available at http://global-data.mars.asu.edu/bin/themis.pl). The BTR provides a scaled temperature value where the true temperature is equal to the pixel value multiplied by a scaling factor plus an offset, both values are provided in the header of each image. We applied the scaling and offset to the BTR data to get the temperature and then used regions of interest to sample the craters, ejecta, and intercrater plains of craters with and without SDE.

2.4. Crater Counting Methods

[17] Crater count ages are based on the crater production functions described by *Hartmann* [2005] to remain consistent with the crater counts and model ages derived by *Baratoux et al.* [2007]. Craters are grouped in incremental size bins to provide a crater frequency for each size range. We then scale the established 3.5 Gy isochron described in column 7 of Table 2 in *Hartmann* [2005] to match the crater frequency data. The following equation taken from *Hartmann* [2005]:

$$N_{D>1\ km} = 5.44\left(10^{-14}\right)\left[\left(e^{6.93T}\right) - 1\right] + 8.38\left(10^{-4}\right)T \qquad (2)$$

where T is the modeled age of the isochron (in Ga) and N is the density of craters larger than 1 km, shows the scaling relationship between the crater density of a surface 3.5 Ga old and of any younger surface. Model ages are determined by selecting the isochron age rescaling from a least squares fit to the crater size-frequency distribution (SFD). Additionally, we compare the crater densities to the standard N(5) and N(2) crater density bins developed by *Tanaka* [1986] to show consistency with this counting record. N(n) densities give the number of craters larger than (n) km in diameter that would form in 1 million square kilometers from a certain Martian geologic time.

[18] Crater counting was performed using CRISM multispectral images and OMEGA observations with MGM results to provide both a comprehensive view of Syrtis Major and to take advantage of the highest spatial resolution VNIR data available. We choose to use the CRISM multispectral data as our counting base map to ensure that we did not count craters for which we could not resolve the presence of SDE. The CRISM-specific MGM was applied to multispectral strips in the Syrtis Major region to produce maps of relative pyroxene composition. These maps were used in conjunction with single wavelength CRISM images to record the diameter and SDE presence of all detectable craters. All valid images were individually reviewed to record craters appearing in a single wavelength grayscale CRISM image. A qualitative inspection of multispectral strips found that band 6 (1.2505 μm) often had fewer artifacts than other bands, so it was consistently used to detect the craters in the mapping strips. We recorded the presence of SDE, its diameter, crater location, and crater diameter. SDE was defined as being present when the area adjacent to the crater had a pyroxene concentration with at least 10% more HCP than the area outside the SDE; however, most instances show between 20 and 30% more HCP. With the CRISM mapping strip resolution of ~200 m/pixel, craters below 600 m in diameter were not resolved and thus are not part of the analysis. Craters smaller than 600 m with SDE were easy to detect unlike craters without SDE, so including craters below 600 m would have led to a sampling bias. Figure 5 shows examples of how craters appear in MSP images and how SDE appears in the associated MGM results.

[19] The OMEGA results provided regional coverage that was merged with CRISM mapping results to produce a combined pyroxene map (Figure 6). CRISM data was scaled by an addition of 0.144 to all values to match mean values to that of OMEGA data for comparison. Scaling was required by inherent differences between the CRISM and OMEGA instrumentation resulting in the consistent shift in MGM values. This scaling factor was determined by finding the difference in (LCP/(LCP+HCP)) values between the OMEGA and CRISM data in the Syrtis Major region of interest. This study focused on relative changes in the MGM results, while specific values depend heavily on end-members used and data calibration and used sparingly for results and conclusions. The OMEGA observations were overlain on top of 256 pixel per degree Mars Global Digital Image Mosaic (MDIM) data to determine crater diameters [*Kirk et al.*, 2000]. This yields roughly 200 m/pixel resolution, similar to that of the CRISM mapping strips. The lower resolution of the OMEGA MGM results only affects the

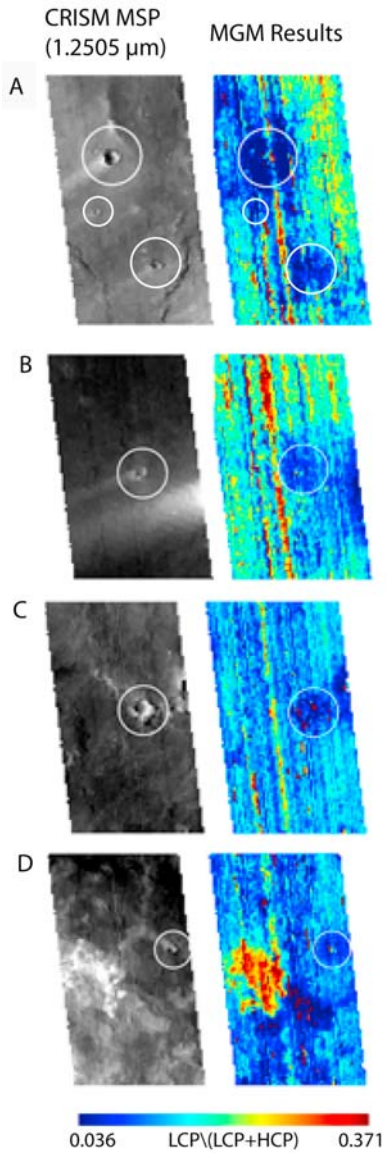

Figure 5. Examples of projected MSP images showing crater with SDE and the corresponding MGM maps. All craters detectable in the grayscale MSP images were counted then checked in the MGM maps for related SDE. (a and b) Taken from MSP00003ACB_05. (c and d) Taken from MSP000041C0_07. Vertical striping is due to column-dependent variations in detector elements.

determination of the SDE diameter and not the crater diameters used for dating.

[20] Crater statistics for all craters larger than 2 km in diameter in our region of interest allowed us to confidently compare our counts with previous work [*Hiesinger and Head*, 2004]. Four populations were plotted: (1) all craters within the region of study with diameters of 2 km and larger which includes craters with SDE and without, (2) craters in the study area with diameters larger than 2 km and that have SDE, which are a subset of the previous count, (3) all craters visible in the CRISM mapping strips, and finally (4) the crater in the mapping strips with SDE, these again are a subset of the previous set.

[21] Our counts are designed to date two events. The counts of all the craters date the age of the Syrtis Major formation. This emplacement of volcanic material covered any preexisting craters creating a crater-free surface. The count of all the craters on this formation can be related to crater production functions [*Hartmann*, 2005] to determine the amount of time required to create the observed crater frequency. The second population of craters with SDE is a subset of the total crater population. Just as a later resurfacing event would cover the old craters and reset the crater retention age, we suggest that the craters with SDE are the craters that occurred following an event that modified the spectral signature of the surface. In this case the frequency of craters with SDE represents the crater population produced in the time since this event. This assumption that craters with SDE represent all the craters since a spectral modification event is supported by several observations made by this and previous work. *Baratoux et al.* [2007] performed crater counts on ejecta blankets of specific large craters and found that all large craters with SDE are younger than any of the craters without SDE. We also observe that the crater frequencies are generally consistent with a specific age isochron independent of diameter. This is most consistent with a population representing a particular age. One note of caution is that while Syrtis Major is considered one of the best exposed regions on Mars, SDE's appear to be more frequent on the eastern side of Syrtis Major. This is largely due to higher dust contents and lower OMEGA resolutions on the west side of Syrtis Major, hampering the ability to detect SDE.

3. Results

3.1. Spectral Properties

[22] MGM modeling was used to generate a regional-scale map showing that many of the craters in Syrtis Major have spectrally distinct eject (Figure 6). In addition, the spectral data of a few select areas were examined to further understand the properties of the spectra that the model is discriminating as HCP and LCP and to try to understand the spectral properties of the subsurface.

[23] Utilizing the highest spatial and spectral resolution possible, we analyze the SDE captured in CRISM image FRT0000818D. This image (Figure 7) measures the edge of a SDE deposit at 18 m/pixel. Spectral ratios (Figure 7b), where the region of interest were divided by a background region to reduce systematic artifacts and highlight the spectral features of interest, show that the SDE has a stronger 2 μm HCP absorption and 1 μm olivine absorption than non-SDE. There is also a possible absorption near 0.5 μm that we will discuss later and may be related to ferric oxide.

[24] An effort to identify SDE terrain in nonimpact related targets focused on a CRISM image of the mildly sinuous channel Arnus Vallis in Syrtis Major (Figure 8a). This feature provides exposed topographic relief that would have been subject to wind erosion. MGM results of this scene show a strong HCP signal concentrated in particulate material that has collected in the trough of the channel (Figures 8c and 8f). This material is likely to be freshly eroded from the channel wall and the particulate nature would result in the strong absorptions comprising the SDE-like detection. Regions of interest average spectra (Figure 8b)

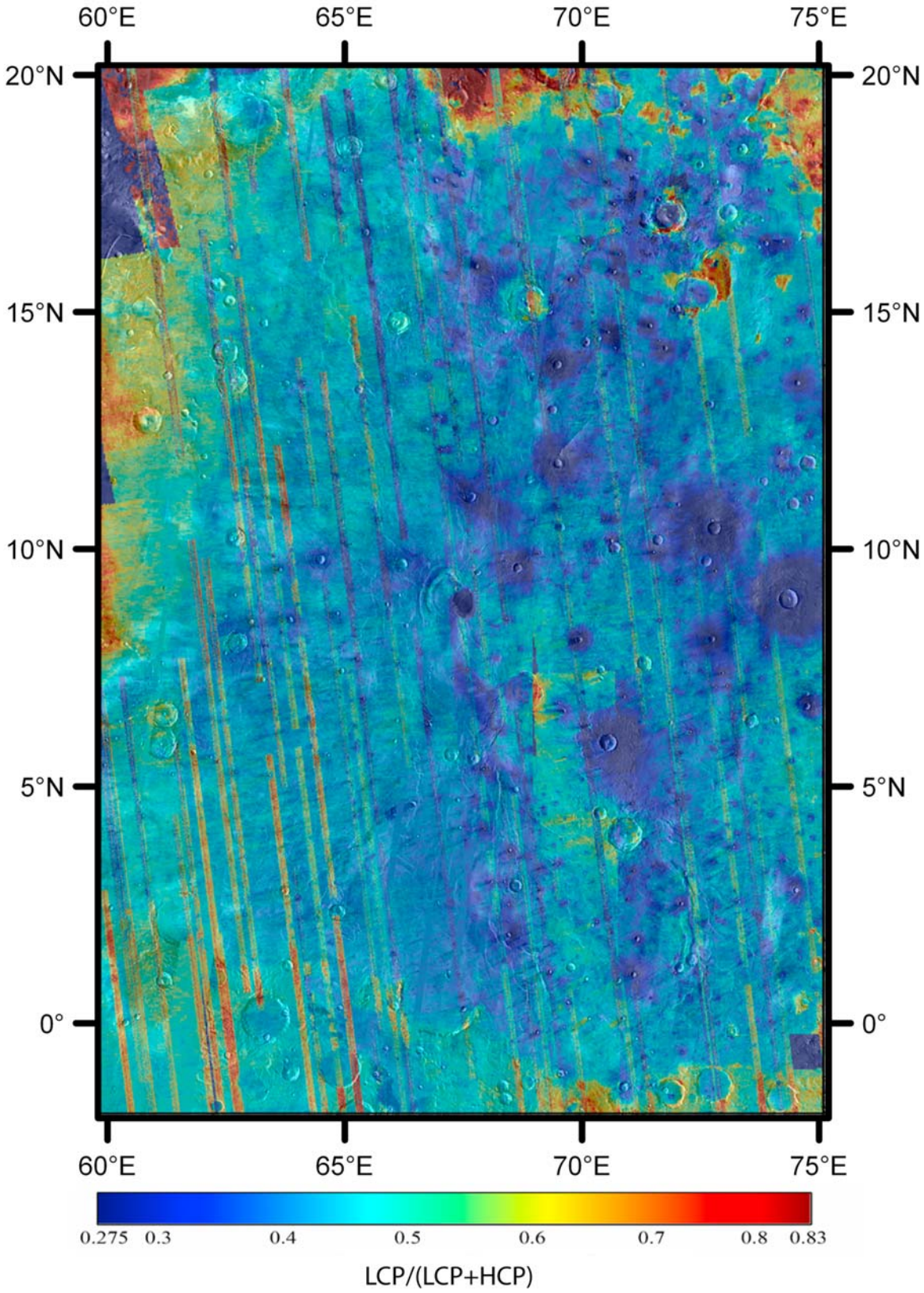

Figure 6. MGM mosaic of Syrtis Major region of interest. OMEGA MGM map overlaid on a THEMIS day IR map, with CRISM MGM results filled in where good MGM coverage exists. Color bar represents values of LCP/(LCP+HCP), where blue indicates HCP enrichment. CRISM MGM results were scaled by an addition of 0.144 to all values to match mean values to that of OMEGA MGM data for comparison. Scaling was required by inherent differences between the CRISM and OMEGA instrumentation resulting in the consistent shift in MGM ratio values.

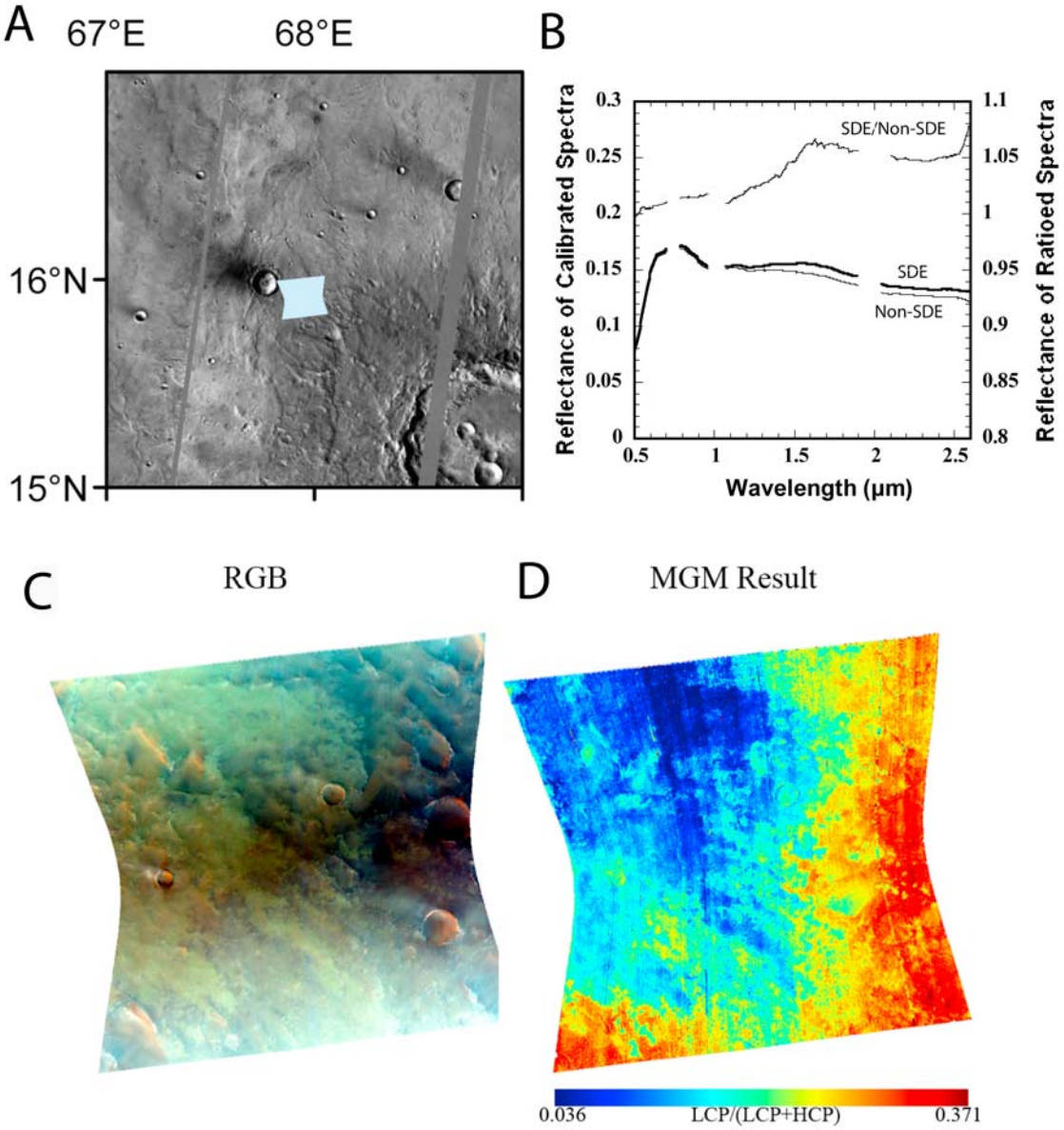

Figure 7. CRISM full-resolution spectra of SDE from FRT0000818D. (a) Context image showing position of FRT observation covering the SE portion of the crater's ejecta blanket. THEMIS day IR in the background. (b) Regions of interest of each spectra type were compared to determine spectra differences. The SDE and non-SDE regions are represented by ~16,000 pixel regions centered on the type label. The top spectra is the ratio of SDE to non-SDE to show the spectra differences. Absorptions in this spectra show features that are stronger in the SDE than the non-SDE. There is a 2.3 μm HCP absorption, a broad 1 μm olivine and pyroxene absorption, and a possible absorption near 0.5 μm. (c) False color (R, 2.47 μm; G, 1.5066 μm B; 1.08 μm) showing the SDE as pale green lobes coming from the upper right corner of the image. (d) MGM results, where scale has been adjusted to bring out differences, although all values are enriched in HCP. CRISM image FRT0000818D. Context image background is THEMIS day IR mosaic [*Christensen et al.*, 2004].

are shown in Figure 8e (top). The red spectra of the channel outcrop is similar to the cyan background non-SDE terrain. The black region of interest is seen as SDE-like in the MGM (Figure 8c) and appears to have a much stronger 1 μm olivine absorption and a better defined 2.1 μm pyroxene absorption. In Figure 8e (bottom), we focus on the near infrared to identify the difference between the SDE-like black spectrum and non-SDE-like red spectrum. The dotted spectrum was created by adding a blue sloped scaling factor to the black SDE spectra, indicating that the difference between SDE and non-SDE can be caused by the addition of a blue spectral slope. Processes capable of adding a spectral slope will be addressed in this paper's discussion.

[25] Another spectra feature seen in the SDE-like material is a visible absorption at 0.53 μm. This absorption in the SDE-like particulate material is a consistent feature mappa-

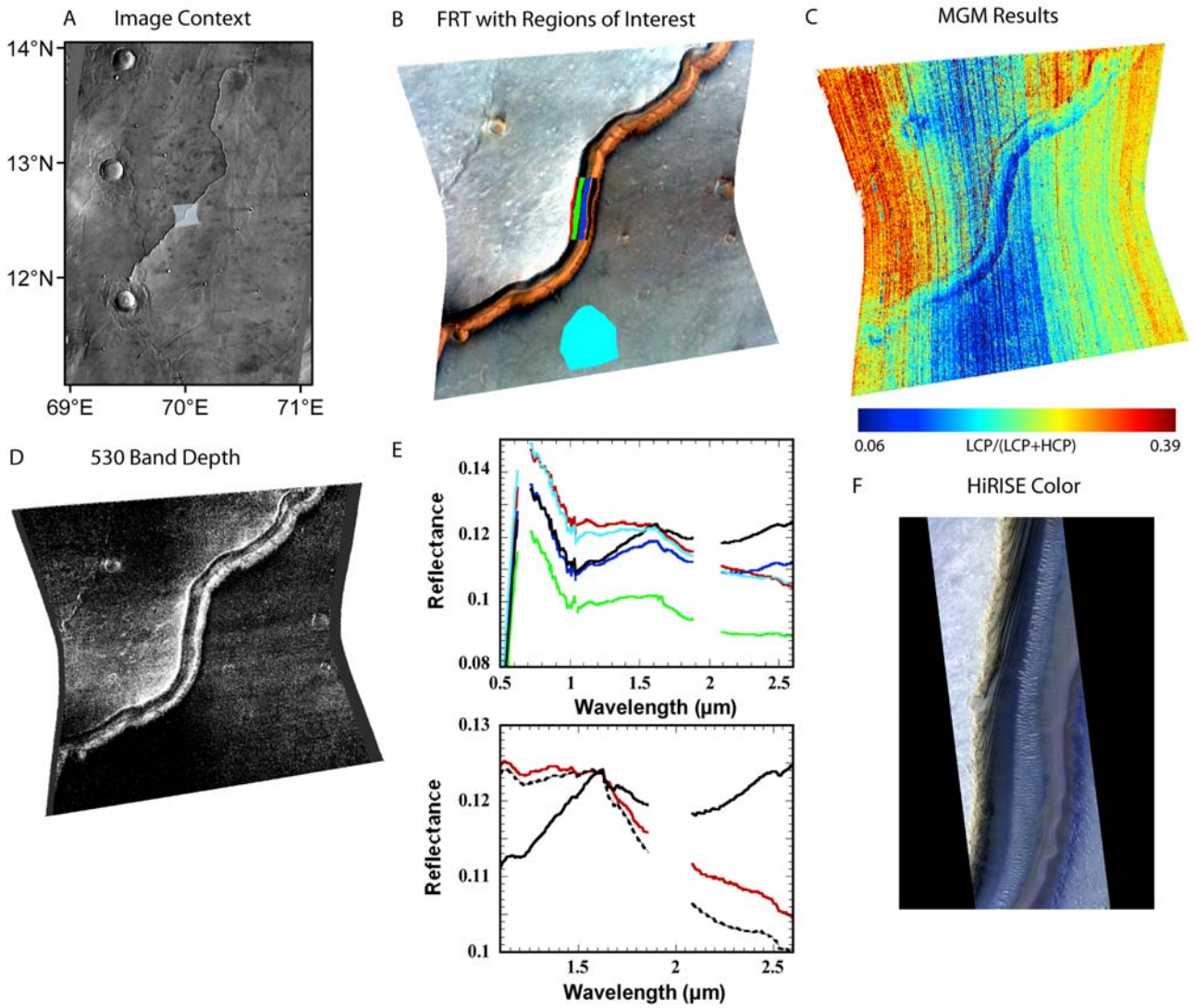

Figure 8. CRISM observation FRT00009D02. (a) Regional context of image covering Arnus Vallis in Syrtis Major. (b) Image with spectral regions of interest and area of HiRISE image PSP_007187_1925 shown in Figure 8f. (c) MGM results of LCP/(LCP+HCP). Strips caused by image noise. High HCP proportion is mapped to the right side of the channel. (d) 0.53 μm band depth map of image. Bright areas are high parameter values and occur in the fine particulate material in the channel associated with the deep blue MGM values and on a thin strip on the western rim of the channel. (e) Spectra from regions of interest in Figure 8b are shown on the top. Red and green are non-SDE surfaces and black is a SDE-like surface. Red and Black from top are shown on the bottom. Dashed line is black with the addition of a scaled blue slope showing that the non-SDE spectra can be created by adding a blue slope to the SDE spectra. Spectral region removed near 2 μm due to CO_2 absorptions. (f) Color HiRISE image PSP_007187_1925 showing details of channel.

ble by the 530 μm band depth parameter (Figure 8d) as defined by *Pelkey et al.* [2007]:

$$1 - (\mathrm{R530}/(\mathrm{a*R648} + \mathrm{b*R440})) \quad (3)$$

where b is (R530)–(R648)/(R709)–(R440) and a is 1–b. This parameter is used to identify absorptions characteristic of crystalline ferric minerals such as hematite and ferric oxides and corresponds to the areas of high HCP in MGM results from the Arnus Vallis images, but it is less clearly expressed in CRISM images of SDE near impact craters. FRT0000818D shows no variations in the 530 band depth while another image, FRT00007D0F, shows a clear enhancement in the 530 band depth at the edge of its SDE. If the 0.53 μm absorption is in fact a property of SDE, it is characteristic of ferric oxides and offers another constraint on the difference between SDE and non-SDE.

[26] One final example (Figure 9) focuses on OMEGA observation 0444_3 located in the north central portion of Syrtis Major and includes a region of the highland terrain north of Syrtis Major. The plot in Figure 9 shows the spectral averages of regions of interest of at least 100 pixels. We again see general similarities between the spectra of

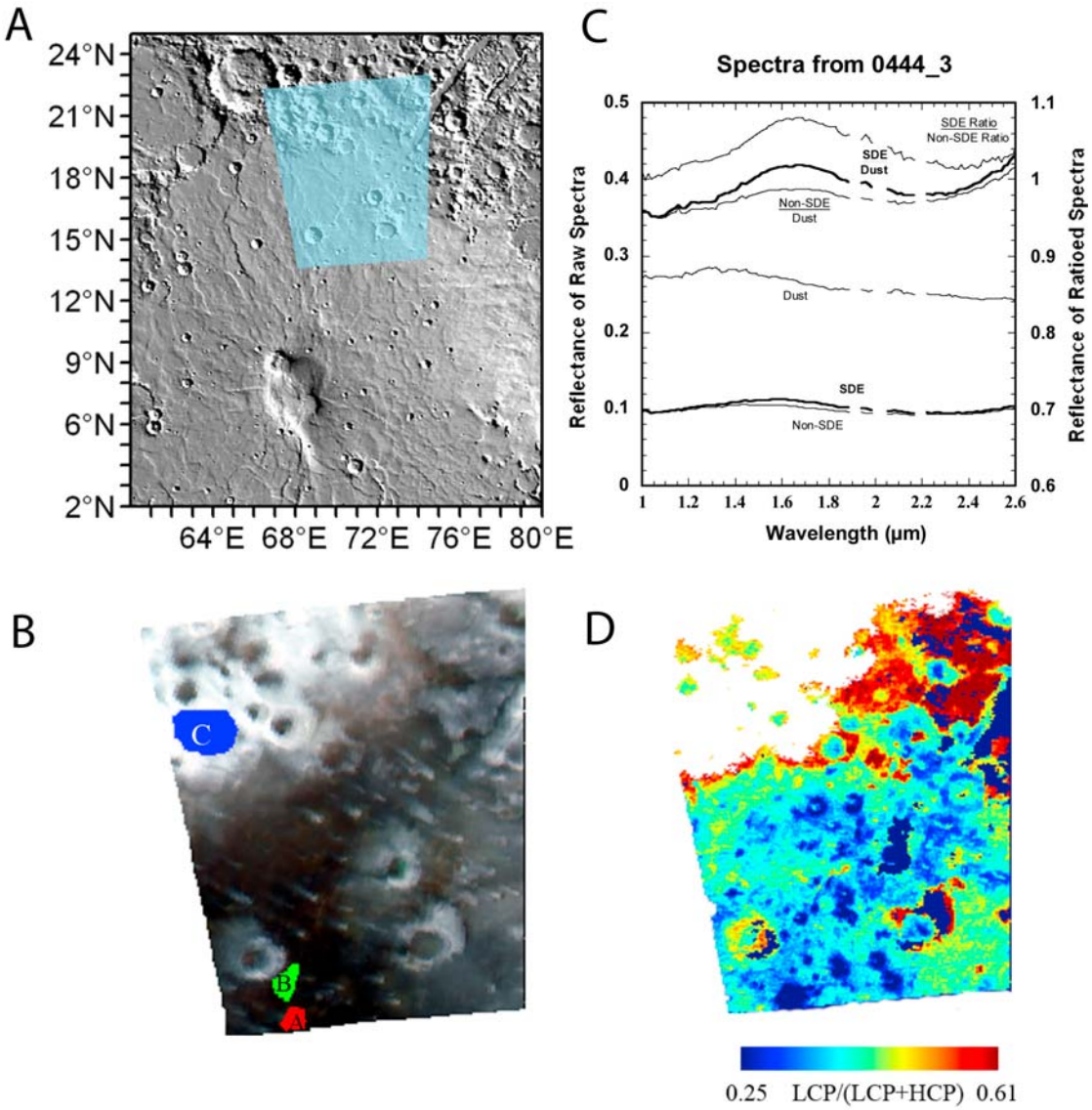

Figure 9. OMEGA 0444_3. (a) Regional context of image covering the northern part of Syrtis Major and parts of the Noachian highlands. (b) RGB false color composite of image with locations of regions of interest. Region A is the SDE spectrum, region B is the non-SDE region, and region C is the dusty region. R, 2.5 μm; G, 1.5 μm; B, 1.1 μm. (c) SDE, non-SDE, and dust taken from regions A, B, and C, respectively. The SDE and non-SDE spectra were divided by the dust spectra to remove nondistinct mineral features. These two were then ratioed to bring out the spectral differences with the difference being the SDE has a 2.3 μm HCP absorption and a combined 1 μm olivine and HCP feature. (d) MGM results of image. Dark blues are modeled with high HCP context; the light blue, cyan, yellows, and reds have increasing LCP modeled in the spectrum because of a broader, more shallow absorption.

SDE and non-SDE, with the SDE having a slightly deeper band depth. We also include a dust spectrum taken from the highlands to show a spectrally band area. Both SDE and non-SDE spectra were divided by the dust spectra to bring out the unique properties. When the SDE is divided by non-SDE we again see the primary difference is that the SDE has significant 2.3 μm HCP absorption and a broad 1.2 μm absorption that is a combination olivine and HCP absorption. This shows overall stronger mafic mineral absorptions due to HCP and olivine. This is consistent with previous reports of the presence of significant amount of olivine in different crater ejecta of this region [*Poulet et al.*, 2009b].

3.2. TES Results

[27] Observations from the Thermal Emission Spectrometer (TES) instrument [*Christensen et al.*, 1992] were used from TES orbit 6012 that covered the area of four separate SDE regions and two non-SDE regions. Dividing the SDE average spectra by the background spectra (Figure 10) yields a featureless line, indicating no spectral variation between the SDE and the non-SDE background. In addition, linear deconvolution of the areas was preformed and differences between the SDE and non-SDE site were generally less than the inherent error. These observations constrain the

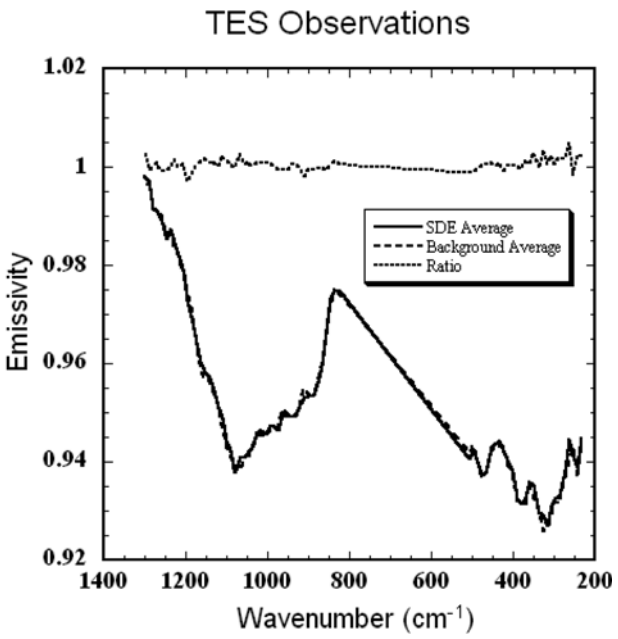

Figure 10. Atmospherically corrected TES spectra from several locations within SDE and of the Syrtis Major background. Spectral plot of the average of four SDE locations covered by TES orbit 6012 and two background locations. Each spot is a 3 × 3 TES pixel average. The averaged spectra of the two regions are very similar, indicating there is no spectral difference between the SDE and non-SDE regions in the thermal infrared.

nature of the difference between the regions. The mineralogical difference predicted by VNIR data should result in a measurable difference in the TIR if it is due to bulk mineralogical differences. The differences in the spectral properties of SDE and non-SDE between the VNIR and TIR may be caused by the slight difference in sampling depth of the wavelength regions, effects of a rind or coating, or grain size effects. The large spatial regions that are seen as SDE and non-SDE in OMEGA observation should allow the low spatial resolutions of the TES instrument to observe the difference if it is was there. The fact that the distinct VNIR SDE is not seen in TIR must be considered in any explanation for SDE.

3.3. THEMIS Results

[28] A qualitative assessment of the craters in Syrtis Major with THEMIS night IR imagery shows that all of the craters with exceptional brightness temperatures, taken as the freshest, have some sign of SDE. Brightness temperature is sometimes used as a proxy for age, since THEMIS bright regions have higher thermal inertia than dark regions. High thermal inertia indicated more rocky terrain, such as the rim and ejecta of a fresh crater that has not had time to fill in with sand and finer grain material. However, there are many examples of craters that are not noticeably brighter in the night IR images yet still have SDE. This illustrates two main points: first that all the bright young craters display SDE, indicating that SDE is seen on all the craters qualitatively determined to be young, and second that the cause of the SDE detection is not a property that is completely correlated with nighttime temperature. A more quantitative comparison was performed for six craters, three with SDE and three without and is shown in Table 2. For each crater we use a single THEMIS image to keep the temperatures comparable. We record four temperatures for each crater, the average temperature within and including the crater rim, the average of just the ejecta blanket, the average of both those regions, and finally a comparable region away from the crater that contains no SDE. We see a clear decrease in temperature from the crater to the other regions. This is explained as the bedrock exposed in the crater rims and peaks retains more surface heat than more granular material of the ejecta and intercrater plains over the course of the day. When we compare the ejecta to the non-SDE plains, we see that the values are consistently within the standard deviation. There is no systematic difference between the SDE and non-SDE ejecta. This supports the conclusion stated above that physical properties as expressed in thermal data cannot alone explain the difference between SDE and non-SDE terrain.

3.4. Counting Craters With Spectrally Distinct Ejecta

[29] Mars geologic time has been broken up into three eras: Noachian (Early, Middle, Late), Hesperian (Early, Late), and Amazonian (Early, Middle, Late) [*Tanaka*, 1986], defined using crater densities with a given number of craters of a certain size range per 10^6 km^2 of surface area. The entire Syrtis Major region of interest has an area of 1,068,000 km^2, while the area covered by valid CRISM MGM results is 402,000 km^2, or 37.6% of the total area of our region of interest. Our counts (Figure 11) of all the craters in Syrtis Major yield 205 craters larger than 5 km in diameter (N(5) age). This scales to 191 craters per 10^6 km^2, fitting in the 125–200 range bin of the Early Hesperian age [*Tanaka*, 1986]. Using the *Hartmann* [2005] crater counting chronology for all craters larger than 2 km, this indicates a

Table 2. Table of THEMIS Nighttime Temperatures Comparing SDE and Non-SDE Craters[a]

THEMIS ID	Latitude	Longitude	Diameter (km)	Type	Crater Rim T (SD)	Ejecta T (SD)	Ejecta+Crater Rim T (SD)	Background T (SD)
I16904012	8.06N	69.96E	7.6	SDE	225.32(5.2)	224.61(2.7)	224.99(3.7)	224.68(1.7)
I18027013	6.66N	74.79E	7.3	SDE	231.62(5.0)	229.93(2.5)	230.28(3.2)	230.93(1.5)
I19250003	13.5N	74.5E	7.7	SDE	229.83(4.4)	227.72(1.6)	228.31(2.9)	226.23(1.4)
I06670013	13.04N	72.69E	10.3	Non-SDE	185.52(5.2)	182.55(2.6)	182.85(3.2)	181.9(2.8)
I16904012	10.44N	69.56E	12.9	Non-SDE	226.13(4.5)	222.79(2.5)	223.71(3.5)	223.09(1.6)
I06620011	6.47N	75.38E	15.5	Non-SDE	191.4(4.6)	187.30(2.6)	188.57(3.8)	188.6(2.3)

[a]Columns list THEMIS image ID number, crater location, crater diameter, crater type (SDE or non-SDE), the average temperature of the crater rim and interior, the ejecta blanket only, the combined ejecta, rim, and interior, and a nearby non-SDE background plains area.

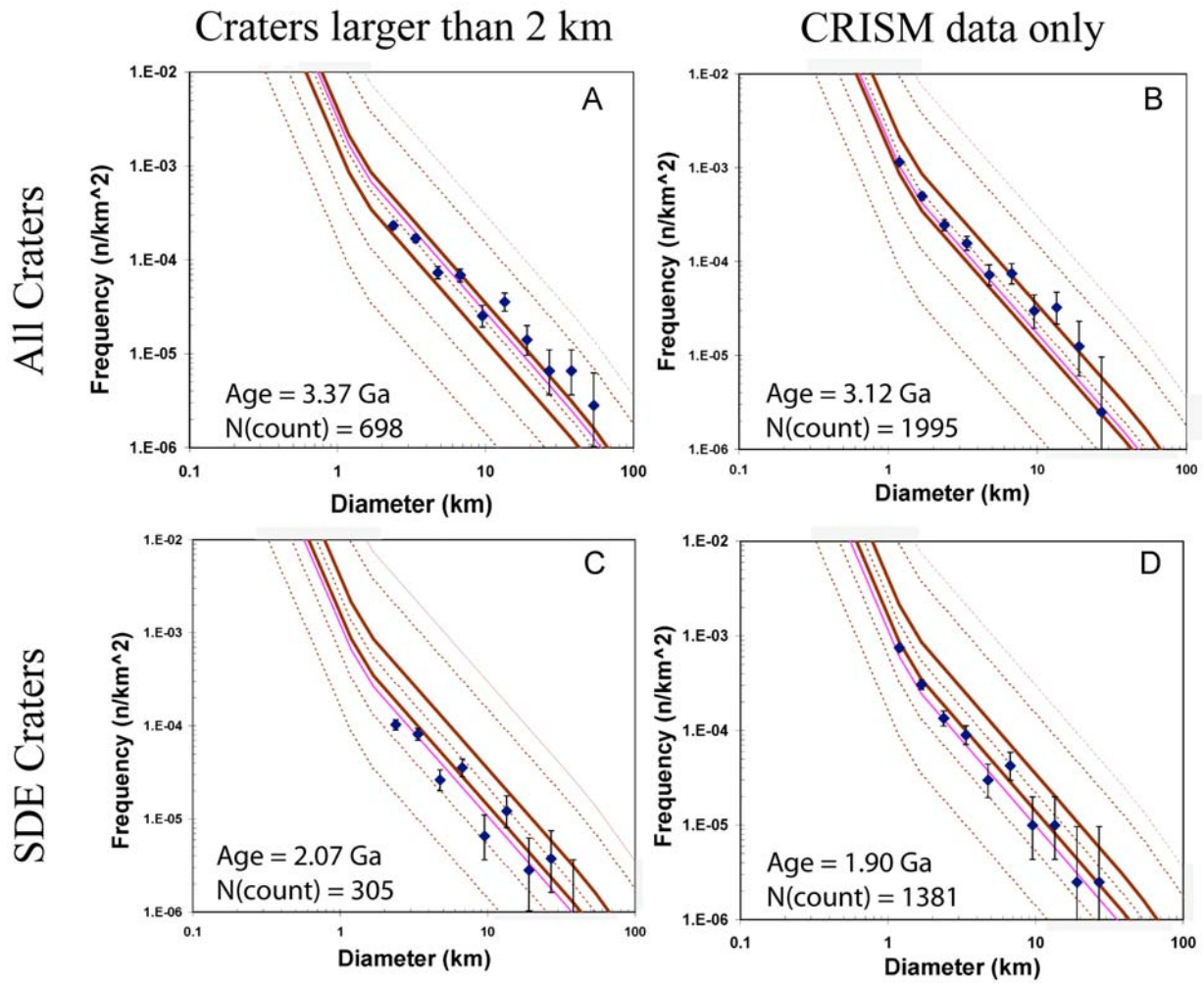

Figure 11. Syrtis Major crater counting results plotted on incremental diagram. (a) Combined CRISM-OMEGA count of all craters larger than 2 km in diameter in our region of interest. (b) Counts of all the Syrtis Major craters seen in valid CRISM produced MGM mapping strips. (c) Counts of Syrtis Major craters with SDE above 2 km in diameter using combined CRISM-OMEGA data. (d) Counts of craters with SDE from CRISM mapping strips only. The 2004 Hartmann isochron iteration [*Hartmann*, 2005].

model age of 3.37 Ga for the volcanic formation. When we compare this age to the age of all the craters counted only on the CRISM mapping strips, we get a slightly younger age of 3.12 Ga, yet still in the Early Hesperian. The younger age is likely the result of the 10 km wide images undersampling large craters, since the large craters were not always seen in the limited multispectral coverage. This specific bin examples show a fit at a particular size bin, the plots in Figure 11 show that the crater size distribution fits specific model age isochrons for a wide range of diameters. These results compare favorably with the results published by *Hiesinger and Head* [2004] and confirm our ability to use CRISM imagery to reproduce a previously preformed crater count.

[30] Counts of craters with SDE yield a total count of 306 craters larger than 2 km in diameter (N(2) age), scaling to 287 per 10^6 km^2, and fitting into the 150–400 range for the Early Amazonian [*Tanaka*, 1986]. These counts give an age of 2.07 Ga, close to the 2 Ga transition age proposed by *Baratoux et al.* [2007]. Analyzing only CRISM data of craters with SDE we get an age of 1.9 Ga. This model age is most consistent for craters between 2 and 10 km in diameter. Above and below this size range, the model ages correspond to a slightly younger timeframe, possibly caused by the large crater under sampling and small crater erosion.

[31] Early geologic maps of Syrtis Major, derived from Viking Orbiter images [*Greeley and Guest*, 1987] listed the age of Syrtis Major in the Late Hesperian based on crater counting. Later counts refined the age of Syrtis Major to the Early Hesperian [*Hiesinger and Head*, 2004], which is consistent with our modeled age. The counts of craters with SDE indicate an age near the Hesperian-Amazonian boundary for craters with diameters between 2 and 10 km, in agreement with *Baratoux et al.* [2007]. Younger ages indicated from the smaller craters are likely due to the faster rate that smaller craters erode, are covered, or otherwise have their distinct spectral signature erased [*Hartmann*, 2005]. Since the age of enriched craters is consistent over a large size range it implies that there is a chronologic transition from nonenriched to enriched craters and that it is not a function of crater size or impact processes.

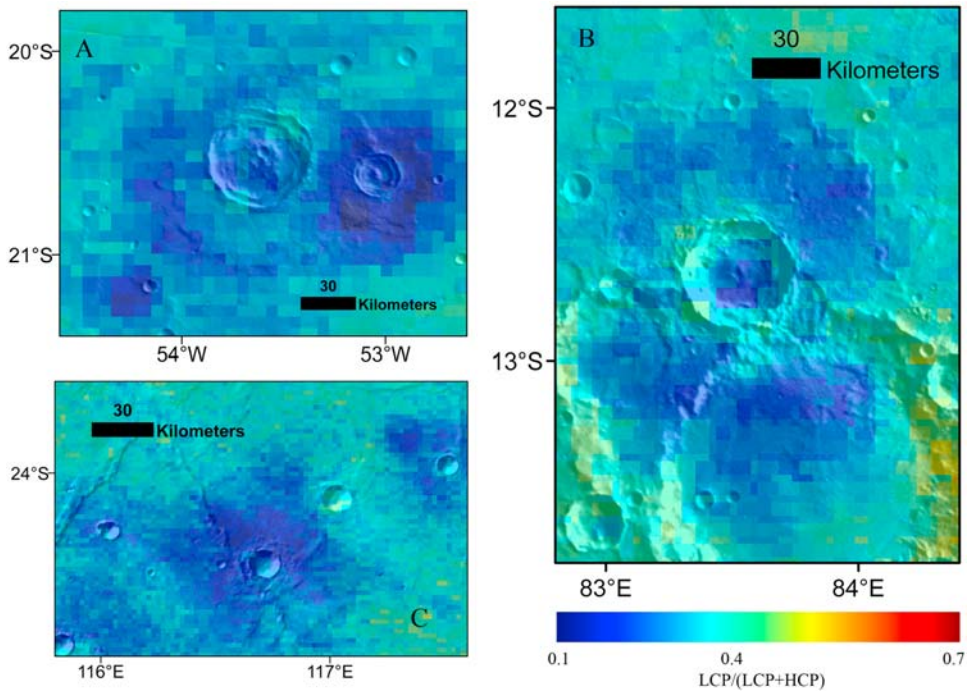

Figure 12. Examples of craters with enriched ejecta not in Syrtis Major north is up in all images. (a) Cluster of craters with SDE ~270 km to the south of the eastern edge of EOS Chasma. Two largest craters near center of image have SDE, as does the small crater in the southwest corner. (b) Terra Tyrrhena. (c) One of two craters in Hesperia Planium with SDE. (Analysis done with OMEGA data overlain on a THEMIS DayIR mosaic [*Christensen et al.*, 2004].)

3.5. Spectrally Distinct Ejecta Outside of Syrtis Major

[32] To test if SDE are unique to Syrtis Major, we analyzed OMEGA observations in other regions on Mars with a high background HCP values. We observed craters with SDE in on the plains about ~250 km to the south of western Eos Chasma (Figure 12a; 20.5°S, 53.5°W), in Terra Tyrrhena (Figure 12b; 12.7°S, 83.5°E), and Hesperia Planium (Figure 12c; 24.3°S, 116.8°E). At OMEGA resolutions with an incomplete mapping of the above regions we have identified at least a dozen craters with SDE in the combined regions (example in Figure 12). The location south of Eos has two large well-exposed craters with SDE clustered along with a number of smaller craters, that border on the limits of OMEGA resolution. Hesperia Planium has several well exposed craters with SDE, while the Terra Tyrrhena region has at least one. However, only a few craters with SDE, we are unable to date the transition in these areas by crater counting of the population on the ejecta blanets. Nevertheless the presence of SDE indicates that the process responsible for altering the spectral signature may be widespread.

4. Discussion

4.1. Spectrally Distinct Ejecta Constraints

[33] Our analyses reveal several lines of evidence and constraints that must be satisfied to explain the formation of SDE. First, the process must affect the VNIR spectral properties of the surface so that the SDE appears to contain a higher relative proportion of HCP than the background material. This may result from an actual change in the proportion of HCP relative to the background material or by modifying the spectral properties of the non-SDE regions such that the MGM predicts relatively more LCP. Inspection of the spectra show that SDE consistently has stronger HCP and olivine absorptions than the non-SDE, and may have a 0.53 μm ferric oxide absorption not seen in the non-SDE surfaces. While the non-SDE terrains still have the mafic absorptions in unratioed spectral data, the band strengths are significantly weaker than the SDE regions. Second, the difference between the SDE and background material is observed in the VNIR but not the TIR. This could be caused by a difference in sampling depth, mineral percent thresholds, textural considerations, or wavelength sensitivity. Third, in Syrtis Major, SDE only appears around craters formed from the Hesperian-Amazonian boundary to the present. This indicates that the formation mechanism is related to a geologic or environmental change that occurred ~2 Ga. Finally, the observation of SDE in other terrains throughout Mars may indicate that they are a global feature and that they were caused by a global-scale process and not limited to Syrtis Major.

4.2. Significance and Implications of Spectrally Distinct Craters

[34] Crater counts of individually selected craters show that craters with SDE are systematically younger than craters without SDE. Crater counts model the transition from craters without SDE to craters with SDE at ~2.1 Ga, just after the Hesperian-Amazonian geologic boundary. That the transition coincides with this boundary and that these features are widely distributed compel us to consider

possible explanations at both the local and global scale. One scenario is that differences are due to changes in pyroxene compositions of Syrtis Major's lava and that the transition marks the time when craters impacting into Syrtis Major begin to excavate material enriched in HCP. A second scenario is that Syrtis Major has always had a bulk composition more similar to that of the SDE than the typical current surface and the transition marks the end of a surface modification process that altered the surface. The second scenario could have been either a single dramatic event, such as the emplacement of a surface mantling material or a single alteration event, or a gradual change in environmental conditions from ones that erased the SDE signal to conditions where it is preserved.

[35] For the first scenario, we consider changes that could affect all of Syrtis Major so that only the most recent craters excavate SDE. One possibility is that a late stage volcanic process deposited an edifice-wide HCP-rich sill below the surface. This sill would need to exist throughout the entire 1100 km wide region and within 50 m of the surface so that the smallest resolvable craters can excavate into it, and not fill in the old craters that have several hundred meters of relief. These constraints make such an event implausible. Another possibility is that the bulk of the Syrtis Major edifice shares the composition of the SDE, and late stage volcanism covered the surface with flows with more moderate HCP values. However, without very low viscosity lava, it seems unlikely that enough material could be erupted to cover the region without resetting the modeled crater count age. Ashfall is another possibility, that would require a source coupled with a wind regime that would allow coverage of the entire edifice after the last volcanic flow deposits. No ash source has been identified and such a deposit would have subdued the sharp mineralogical boundary visible between the Hesperian and Noachian terrains. In addition, clearly identifiable morphologic features consistent with lava flows are present in visible imagery and inconsistent with ash deposits. A final possibility for this scenario is that the impacts are excavating a buried lava flow of SDE composition. Since we observe craters with SDE ranging from the tens of kilometers to the hundreds of meters, it is difficult to reconcile the geometry of this layer with the existing craters with SDE. In addition, this would not explain the systematically younger ages of the craters with SDE.

[36] For the second scenario, mechanisms must be considered in light of known constraints. Possible mechanisms must modify the spectral properties of the 2 μm absorption feature of the background materials to be modeled as a shift to a shorter wavelength and decrease its band depth, since this is the essential spectral difference seen between the SDE and the background.

[37] First, we consider short-term single events that could have reset the modeled enrichment age. *Grizzaffi and Schultz* [1989] report that a thick deposit of volatile rich sediment in the Isidis Basin was removed close in time to the Hesperian-Amazonian boundary. If this material became airborne and followed current wind patterns, as seen in Syrtis Major wind streaks, it would have blown west toward Syrtis Major. Deposition of this material could have modified the surface spectral properties. If this is the material that currently covers most of Syrtis Major, it would have to be spectroscopically consistent with the primary mafic signature seen here in a wide variety of instruments. Instead of just masking the enrichment, volatiles may have been an agent of alteration and reacted with HCP-rich material to produce a material that is modeled as LCP-rich. *Ivanov and Head* [2003] point out that late stage volcanism (Late Hesperian) on the eastern flank of Syrtis Major may have triggered the collapse of the Isidis Basin rim at this location, and could have been related to the release of volatiles from the Isidis deposits.

[38] An alternative possibility for explaining the SDE is that the enrichment diameter decreases with time as local surface erosional processes make the SDE appear more like the background through physical mixing. It is possible that all of the nonenriched craters are simply old enough for the enrichment to shrink to zero. However, it seems that it would take much longer to eliminate the enrichment of large craters than of the smaller ones. Instead, our counts show a fairly consistent modeled age for all sizes indicating that the removal of enrichment is tied to a specific time. Mixing with LCP-rich material from the surrounding Noachian terrains is also unlikely, since particulates are unlikely to evenly spread across Syrtis Major, and the Highlands-Syrtis Major boundary shows a sharp rather than gradual composition change [*Mustard et al.*, 2005]. Large-scale material mixing would blur this boundary. The LCP in Noachian terrains has strong absorption bands that would be apparent instead of just weakening the HCP absorptions. Another possibility is that these craters undergo a steady transition from SDE to non-SDE and 2 Ga is the equilibrium time of transition. If this process is size-independent, it would be difficult to rule out solely from the crater counts but would still be a widespread process of spectral modification.

[39] Finally, we consider possibilities that evoke a climatic shift from one type of environment that may have removed the spectrally distinct signal to one that could not. The late Hesperian is the time of formation of many of the outflow channels on Mars [*Carr*, 2006]. This would have placed massive amounts of water onto the surface which could have frozen, then sublimated into the atmosphere [*Kreslavsky and Head*, 2002]. This could have been the last time the Martian atmosphere hosted significant $H_2O(v)$, which may have reacted with surface rocks to alter the HCP-enriched primary mafic minerals in Syrtis Major.

[40] In addition to the emplacement of Syrtis Major, the Hesperian saw widespread global volcanism, from the formation of the ridged plains that could have covered up to 33% of the surface (the northern lowlands), to much of the formation of Tharsis, Elysium, Alba Patera, and all of Hesperia Planium [*Head and Basilevsky*, 2001]. This widespread volcanism would have released vast quantities of gases into the atmosphere. The release of SO_2 from volcanic sources could have combined with molecules containing O and H to form H_2SO_4 aerosols that may have lead to surface leaching [*Settle*, 1979; *Bullock and Moore*, 2007]. These could have had the effect of altering the HCP-enriched surface of Syrtis Major causing a muted spectral signature leading to the MGM result. In this case, our transition date would mark the time of removal of these reacting agents from the atmosphere to a level where they were insufficient to alter the Syrtis Major surface and mirrors the observations that the Hesperian was a time of sulfate formation

[*Bibring et al.*, 2005]. The HCP enrichment observed in crater ejecta may simply represent relatively fresh material excavated from depth after the alteration process had ceased. The sharp mineralogical boundary seen between the Noachian and Hesperian ages basalts remains due to actual compositional differences in these units.

4.3. Proposed Mechanism of In Situ Surface Alteration

[41] Given the constraints discussed above, we propose that the most consistent explanation for the data is the existence of a thin surface coating or rind on non-SDE surfaces, which is absent on SDE surfaces. That is, all of the rock units were originally SDE-like, with mafic VNIR spectral properties characterized by HCP- and olivine-related absorption features, but were modified in the late Hesperian by surface-atmosphere interactions so as to impart a mild spectral slope and decreased band strengths to the older surfaces. The addition of this subtle slope is enough to modify the MGM pyroxene spectral fits of the relative abundance of LCP versus HCP but not enough to change the overall determination that Syrtis Major is relatively dust free, and composed of pyroxene-bearing basalt. The proposed coating/rind would need to weaken the pyroxene and olivine absorptions, while not affecting the TIR observations from TES. We consider two types of surface coatings studied in the laboratory that may generate these spectral changes: (1) a coating of amorphous silica, analogous to the coatings seen on basaltic rocks in Hawaii and (2) a coating of ferric powder, derived from local soils and dust, deposited on basalt.

[42] Work done by *Minitti et al.* [2007] examined silica coatings that developed on HCP-rich Hawaiian basalts through leaching by low-pH fluids and precipitation of secondary phases. We consider the sample MIO from that study, taken from the Mauna Iki flow field in the Ka'u Desert. *Minitti et al.* [2007] recorded both the VNIR (Figure 13a) and TIR spectra of both the rock interiors and several types of coatings. The basalt interior VNIR spectra are dominated by a well-developed HCP absorption signature and are analogous to observations of Martian SDE. The VNIR spectrum of the least developed 'black' coating from MIO has pronounced ferric absorptions shortward of 0.7 μm and then is strongly downward sloping toward longer wavelengths. It also has a small hydration absorption near 1.9 μm. While the Syrtis Major non-SDE background is not just a spectral slope and

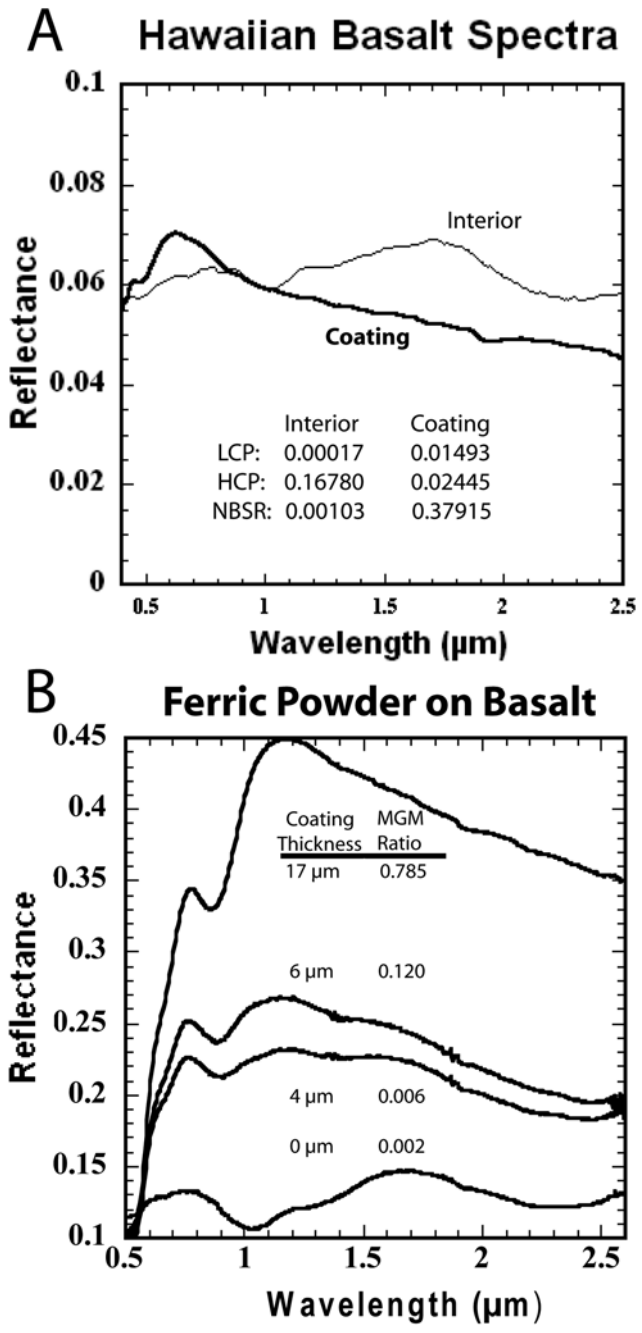

Figure 13. (a) Spectra of Hawaiian basalts sample Mauna Iki Orange (MIO) previously reported by *Minitti et al.* [2007] and publicly available through Brown University's RELAB Spectral Library. MIO Interior shows classic basaltic spectral characteristics with strong broad 2 μm band, shifted to 2.3 μm indicating high proportion of HCP. One μm absorption is like the combination of olivine and pyroxene absorptions. MIO black coating is the spectra of a dark coating on the rock's surface, characterized by a peak near 0.6 μm and a negative slope to longer wavelengths with a shallow absorption near 1.9 μm. These spectra were run through MGM code identical to that used on CRISM observations with the results shown in the inset table, LCP and HCP are the band strengths of the Gaussian used to model the respective component, NBSR is the band strength ratio LCP/(LCP+HCP). The interior is almost completely HCP, consistent with its spectral shape, and the values of the most HCP enriched Syrtis Major terrain. The MGM results for the coating are slightly enriched in HCP, values similar to the Syrtis Major background, despite the lack of a clear pyroxene absorption. (b) VNIR spectra of ferric powder coated basalt slabs along with spectra of an uncoated basalt, measured at i = 30, e = 0 and taken from *Fischer and Pieters* [1993]. Coating thickness is listed next to each spectra along with the result of the CRISM-specific MGM (LCP/(LCP+HCP)). Ferric coating adds a blue slope that would increase the MGM ratio. SDE material would be consistent with 0–4 μm coating, while the non-SDE surfaces would be consistent with a 6–17 μm coating if the trend continues.

does not have a 1.9 μm absorption, it could result from the presence of a thin silica coating (thinner than that in the MIO sample) which adds a spectral slope to the HCP signature causing the absorption to shallow and broaden. However, all the silica coatings examined by *Minitti et al.* [2007] showed very distinctive thermal infrared spectra. Since we do not observe any evidence of silica in the TES observations of Syrtis Major, it means that the silica content is below the TES detection limit of a few percent, or that it does not exist. It may be that the coating only affects the top few microns of the surface so that VNIR observations see the coating even though it does not constitute a significant volume of the TIR observation depth.

[43] Work by *Fischer and Pieters* [1993] using VNIR spectra shows that a thin ferric powder only a few microns thick can also produce a blue-sloped spectrum (Figure 13b) when deposited on top of a basaltic substrate. This is due to two effects. First, thin (few microns) coatings are more opaque at shorter wavelengths and their relative transparency at longer wavelengths means the dark basaltic substrate is more visible. Second, if the coating, e.g., fine powders cemented by reaction with thin films of water, is smooth at the scale of the incident light, preferential forward scattering of longer wavelength light can lead to the blue slope effect in some viewing geometries. While we know of no thermal infrared observations for this sort of coating, it should have minimal effect on the spectra since there would be no appreciable change in composition between the basaltic coating and the basaltic substrate. This effect may be enough to broaden the pyroxene absorptions enough to be distinguished by the MGM analysis.

[44] If the ferric powder coating shown in Figure 13b is the cause of the SDE/non-SDE difference it allows constraints on the thickness of the coating. Figure 13b shows that a 6 μm thick coating is not enough to cause a HCP-rich rock to appear as a non-SDE while 17 μm is too thick and would cover the pyroxene absorptions seen in the SDE terrain. This is consistent with laboratory studies of thermal spectroscopy showing the 10–20 μm thick coatings would have a thermal component while coatings $\sim$100–120 thick completely dominate the thermal infrared [*Johnson et al.*, 2002]. This points to the non-SDE coating having a thickness between $\sim$6 μm and $\sim$10 μm.

[45] From landed missions, there is ample evidence for the existence of coatings and rinds on Martian rocks, which result from a combination of physical and chemical alteration processes [*McSween et al.*, 1999; *Bishop et al.*, 2002; *Hurowitz et al.*, 2006]. The Mars Pathfinder rover with its multispectral imager and APXS instrument made several measurements that could be consistent with the presence of rock coatings. The spectral properties of Mars Pathfinder rocks show two trends, consistent with addition of different ferric oxide minerals [*McSween et al.*, 1999]. The elevated SiO_2 content of rock surfaces compared to typical basalts could also indicate a silica-rich coating, although without the ability to ascertain the composition of rock interiors, the evidence is equivocal [*McSween et al.*, 1999]. The rock brushing and abrasion capabilities of the Spirit Mars Exploration Rover definitively reveal the presence of coatings and rinds on Gusev Crater basaltic rocks. Comparison of brushed and unbrushed surfaces shows that coating by local Gusev soils is common. Following removal of the loose soils and dust by brushing, APXS measurements show the brushed surfaces of the plains basalts Adirondack and Humphrey are depleted in Fe and Mg relative to the interior [*Hurowitz et al.*, 2006]. Brushing and abrasion on Mazatzal shows a multilayer coating, elevated in S, Cl, and ferric oxides [*Haskin et al.*, 2005]. Like Mars Pathfinder rocks, spectral properties of Spirit rocks also reveal changes in spectral slope, absorptions near 900 nm, and depth of a 530 nm absorption feature, all attributed to Fe oxides [*Farrand et al.*, 2006].

[46] *Hurowitz et al.* [2006] propose a multistep process to produce coatings on Martian basaltic rocks, which may also explain their diversity and variation from site to site. First, interaction with an acid fog or acidic fluids at low water-rock ratio initiates mineral dissolution of the most susceptible minerals, olivine for example in the Adirondack class of rocks. Mg^{2+}, Fe^{2+}, and SiO_2(aq) concentrations will increase in solution, leaving a leached rind on the rock's surface in the uppermost microns to hundreds of microns. Evaporation of the solution then results in the precipitation of secondary phases as coatings. Subsequently, soil and dust is added to the rock surfaces.

[47] The dust on the Hesperian basaltic plains in Gusev crater prohibits clear MGM results in this region but if the coating process we hypothesize occurred planet-wide, at or before the early Amazonian, it should have affected the Gusev basalts. Syrtis Major has long been recognized as a low-dust area, so coatings by local soils and dust may play less of a role in obscuring underlying rock compositions here and in other areas on Mars where SDE and non-SDE terrains can be distinguished with MGM mapping. We consider the best analog for the Syrtis Major SDE terrain to be the abraded drill holes on the Gusev plains basalts (Adirondack, etc.): negligibly altered basalt with minimal soil and dust coatings. We consider the Gusev plains brushed surfaces that show evidence of coatings and rinds as analogous to Syrtis Major non-SDE terrains. Like the Gusev basalts, Syrtis Major non-SDE basalts may have been altered by low-pH, low water-rock ratio alteration processes occurring in the pre-Amazonian epoch through interaction with the atmosphere.

4.4. Global Implications for VNIR Observations

[48] The observation of craters with SDE at widely varying locations throughout Mars indicates that the process that caused them may well have been globally occurring. This has broad implications for the use of VNIR observations throughout all of Mars. It will have altered the spectral response from all exposed surfaces older than 2 Ga, which is the vast majority of the planet. The earliest spectral observations of Mars saw Syrtis Major as the best example of actual exposed surface composition [*Adams and McCord*, 1969]. This view has propagated through later spectroscopic observations, but now seems to be unlikely to be as primary as first thought as the majority of the surface is covered by substance causing this spectral modification. While we see no indications that this affects TIR observations it does have a real, if subtle effect on VNIR observations. We suggest that Mars does not have any pristine, unaltered surfaces older than the Early Amazonian. However, it is also important to understand the effects of this on spectral features. Its subtle nature should have limited effects on

strong, sharp absorptions seen in highly altered minerals and would at most cause a mild change to band strength. Similarly the identification of olivine and pyroxenes should not be largely affected, but the strengths and band centers used for spectral unmixing and compositional understanding will be affected as we have seen. We must also consider where it occurs. It has only been identified in regions of high-HCP content; however, we cannot say if this is because it only forms on the rock types located in these areas or if these are then only areas where it can be detected with current methods. Despite the potential to affect all VNIR observations of Mars, it is likely to be significant primarily for studies of broad and weak absorptions, or ones with minor shifts that are used for compositional analysis.

5. Conclusions

[49] The spectrally distinct ejecta (SDE) blankets originally detected and analyzed by *Baratoux et al.* [2007] using OMEGA observations have now been observed with the improved resolution of the CRISM mapping strip data. The higher-resolution data allowed for the observation of a significant number of craters with SDE. Applying crater counting techniques to these observations yields a modeled age consistent with just after the Hesperian-Amazonian boundary (~2 Ga) for the enriched craters. This time frame coincides with many changes to the global and local environment. Late stage volcanism at Syrtis Major is not likely to have caused the transition in itself but could have been a mechanism to liberate the volatiles in Isidis Basin that could have covered the enriched ejecta of the older craters. In addition, many global factors were occurring during this same time frame. The Late Hesperian is the time of the majority of Martian outflow channels that may have released water that froze and then sublimated, hydrating the atmosphere to a level that Mars has not experienced since. This hydration may have had the effect of altering the high-HCP content ejecta to a substance that is modeled as more LCP enriched. The Hesperian was also a time of vast volcanic emplacement, a process that quickly tapered off during the Amazonian [*Head and Basilevsky*, 2001]. The release of volcanic gases, while unconstrained, is believed to have created an atmosphere much different than that of today. This Hesperian atmosphere could have interacted with the surface to create a surface coating that weaken the spectral absorptions in HCP-rich basalts resulting in the mappable spectral difference by age of exposure.

[50] **Acknowledgments.** The work has benefited greatly from the technical assistance and scientific guidance of Leah Roach, the crater counting advice from Caleb Fassett, and the insightful comments of an anonymous reviewer. Additional thanks to the OMEGA and CRISM teams for data acquisition and processing. We gratefully acknowledge NASA's support for the CRISM investigation through the Mars Reconnaissance Orbiter mission. This works is supported by subcontract JHAP852950 from the Johns Hopkins University Applied Physics Laboratory.

References

Adams, J. B. (1974), Visible and near-infrared diffuse reflectance spectra of pyroxene as applied to remote of solid objects in the solar system, *J. Geophys. Res.*, *79*, 4829–4836.

Adams, J. B., and T. B. McCord (1969), Mars: Interpretation of spectral reflectivity of light and dark regions, *J. Geophys. Res.*, *74*, 4851–4856, doi:10.1029/JB074i020p04851.

Bandfield, J. L., V. E. Hamilton, and P. R. Christensen (2000), A global view of Martian surface compositions from MGS-TES, *Science*, *287*, 1626–1630, doi:10.1126/science.287.5458.1626.

Baratoux, D., P. Pinet, A. Gendrin, L. Kanner, J. Mustard, Y. Daydou, J. Vaucher, and J.-P. Bibring (2007), Mineralogical structure of the subsurface of Syrtis Major fom OMEGA observations of lobate ejecta blankets, *J. Geophys. Res.*, *112*, E08S05, doi:10.1029/2007JE002890.

Bellucci, G., F. A. Ltieri, J.-P. Bibring, G. Bonello, Y. Langevin, B. Gondet, and F. Poulet (2006), OMEGA/Mars Express: Visual channel performances and data reduction techniques, *Planet. Space Sci.*, *54*, 675–684, doi:10.1016/j.pss.2006.03.006.

Bibring, J.-P., et al. (1989), Results from the ISM experiment, *Nature*, *341*, 591–593, doi:10.1038/341591a0.

Bibring, J.-P., et al. (2005), Mars surface diversity as reveled by the OMEGA/Mars Express observations, *Science*, *307*, 1576–1581, doi:10.1126/science.1108806.

Bishop, J. L., S. L. Murchie, C. M. Pieters, and A. P. Zent (2002), A model for formation of dust, soil, and rock coatings on Mars: Physical and chemical processes on the Martian surface, *J. Geophys. Res.*, *107*(E11), 5097, doi:10.1029/2001JE001581.

Bullock, M. A., and J. M. Moore (2007), Atmospheric conditions on early Mars and the missing layered carbonates, *Geophys. Res. Lett.*, *34*, L19201, doi:10.1029/2007GL030688.

Burns, R. G. (1970), *Mineralogical Applications to Crystal Field Theory*, 224 pp., Cambridge Univ. Press, New York.

Carr, M. (2006), *The Surface of Mars*, Cambridge Univ. Press, Cambridge, U. K.

Christensen, P. R., D. L. Anderson, S. C. Chase, R. N. Clark, H. H. Kieffer, M. C. Malin, J. C. Pearl, J. Carpenter, N. Bandiera, and F. G. Brown (1992), Thermal emission spectrometer experiment–Mars Observer mission, *J. Geophys. Res.*, *97*, 7719–7734, doi:10.1029/92JE00453.

Christensen, P. R., et al. (2004), The Thermal Emission Imaging System (THEMIS) for the Mars 2001 Odyssey Mission, *Space Sci. Rev.*, *110*, 85–130, doi:10.1023/B:SPAC.0000021008.16305.94.

Cloutis, E. A., and M. J. Gaffey (1991), Pyroxene spectroscopy revisited: Spectral-compositional correlations and relationship to geothermometry, *J. Geophys. Res.*, *96*, 22,809–22,826, doi:10.1029/91JE02512.

Farrand, W. H., J. F. Bell III, J. R. Johnson, S. W. Squyres, J. Soderblom, and D. W. Ming (2006), Spectral variability among rocks in visible and near-infrared multispectral Pancam data collected at Gusev crater: Examinations using spectral mixture analysis and related techniques, *J. Geophys. Res.*, *111*, E02S15, doi:10.1029/2005JE002495.

Fischer, E. M., and C. M. Pieters (1993), The continuum slope of Mars: Bidirectional reflectance investigations and applications to Olympus Mons, *Icarus*, *102*, 185–202, doi:10.1006/icar.1993.1043.

Gendrin, A. (2004), Mineralogie de Mars: L'experience OMEGA., Ph.D. thesis, Université de Paris, Paris.

Greeley, R., and J. E. Guest (1987), Geologic map of the eastern equatorial region of Mars, *U.S. Geol. Surv. Misc. Invest. Map I-1802-B*.

Grizzaffi, P., and P. H. Schultz (1989), Isidis Basin: Site of ancient volatile-rich debris layer, *Icarus*, *77*, 358–381, doi:10.1016/0019-1035(89)90094-8.

Hartmann, W. K. (2005), Martian cratering 8: Isochron refinement and the chronology of Mars, *Icarus*, *174*, 294–320, doi:10.1016/j.icarus.2004.11.023.

Haskin, L. A., et al. (2005), Water alteration of rocks and soils from the Spirit rover site, Gusev crater, Mars, *Nature*, *436*, 66–69, doi:10.1038/nature03640.

Head, J. W., and A. T. Basilevsky (2001), The Hesperian period of Martian history: Key trends in volcanic and tectonic activity, *Lunar Planet. Sci.*, *XXXII*, Abstract 1114.

Hiesinger, H., and J. W. Head III (2004), The Syrtis Major volcanic province, Mars: Synthesis from Mars Global Surveyor data, *J. Geophys. Res.*, *109*, E01004, doi:10.1029/2003JE002143.

Hurowitz, J. A., S. M. McLennan, N. J. Tosca, R. E. Arvidon, J. R. Michalski, D. W. Ming, C. Schroder, and S. W. Squyres (2006), In situ and experimental evidence for acidic weathering of rocks and soils on Mars, *J. Geophys. Res.*, *111*, E02S19, doi:10.1029/2005JE002515.

Ivanov, M. A., and J. W. Head III (2003), Syrtis Major and Isidis Basin contact: Morphological and topographic characteristics of Syrtis Major lava flows and materials of the Vastitas Borealis Formation, *J. Geophys. Res.*, *108*(E6), 5063, doi:10.1029/2002JE001994.

Johnson, J. R., P. R. Christensen, and P. G. Lucey (2002), Dust coatings on basaltic rocks and implications for thermal infrared spectroscopy of Mars, *J. Geophys. Res.*, *107*(E6), 5035, doi:10.1029/2000JE001405.

Kanner, L. C., J. F. Mustard, and A. Gendrin (2007), Assessing the limits of the Modified Gaussian Model for remote spectroscopic studies of pyroxenes on Mars, *Icarus*, *187*, 442–456, doi:10.1016/j.icarus.2006.10.025.

Kirk, R. L., E. M. Lee, R. M. Sucharski, J. Richie, A. Grecu, and S. K. Castro (2000), MDIM 2.0: A Revised global digital image mosaic of Mars, *Lunar Planet. Sci.* [CD-ROM], *XXXI*, Abstract 2011.

Klima, R. L. (2008), Integrated spectroscopy of Mg-Fe-Ca- pyroxenes: A foundation for modern remote compositional analysis of planetary surfaces, Ph. D. thesis, Brown University, Providence, R. I.

Kreslavsky, M. C., and J. W. Head (2002), Fate of outflow channel effluents in the northern lowlands of Mars: The Vastitas Borealis Formation as a sublimation residue from frozen ponded bodies of water, *J. Geophys. Res.*, *107*(E12), 5121, doi:10.1029/2001JE001831.

Langevin, Y., F. Poulet, J.-P. Bibring, and B. Gondet (2005), Sulfates in the north polar region of Mars detected by OMEGA/Mars Express, *Science*, *307*, 1584–1586, doi:10.1126/science.1109091.

McSween, H. Y., Jr., et al. (1999), Chemical, multispectral, and textural constraints on the composition and origin of rocks at the Mars Pathfinder landing site, *J. Geophys. Res.*, *104*, 8679–8715, doi:10.1029/98JE02551.

Minitti, M. E., C. M. Weitz, M. D. Lane, and J. L. Bishop (2007), Morphology, chemistry, and spectral properties of Hawaiian rock coatings and implications for Mars, *J. Geophys. Res.*, *112*, E05015, doi:10.1029/2006JE002839.

Murchie, S., et al. (2007), Compact Reconnaissance Imaging Spectrometer for Mars (CRISM) on Mars Reconnaissance Orbiter (MRO), *J. Geophys. Res.*, *112*, E05S03, doi:10.1029/2006JE002682.

Mustard, J. F., and C. M. Pieters (1989), Photometric phase functions of common geologic minerals and applications to quantitative analysis of mineral mixture reflectance spectra, *J. Geophys. Res.*, *94*, 13,619–13,634, doi:10.1029/JB094iB10p13619.

Mustard, J. F., and J. M. Sunshine (1995), Seeing through the dust: Martian crustal heterogeneity and links to the SND meteorites, *Science*, *267*, 1623–1626, doi:10.1126/science.7886449.

Mustard, J. F., S. Murchie, S. Erard, and J. Sunshine (1997), In situ compositions of Martian volcanics: Implications for the mantle, *J. Geophys. Res.*, *102*, 25,605–25,615, doi:10.1029/97JE02354.

Mustard, J. F., F. Poulet, A. Gendrin, J.-P. Bibring, Y. Langevin, B. Gondet, N. Mangold, G. Bellucci, and F. Altieri (2005), Olivine and pyroxene diversity in the crust of Mars, *Science*, *307*, 1594–1597, doi:10.1126/science.1109098.

Mustard, J. F., et al. (2008), Hydrated silicate minerals on Mars observed by the Mars Reconnaissance Orbiter CRISM instrument, *Nature*, *454*, 305–309, doi:10.1038/nature07097.

Pelkey, S. M., et al. (2007), CRISM multispectral summary products: Parameterizing mineral diversity on Mars from reflectance, *J. Geophys. Res.*, *112*, E08S14, doi:10.1029/2006JE002831.

Poulet, F., and S. Erard (2004), Nonlinear spectral mixing: Quantitative analysis of laboratory mineral mixtures, *J. Geophys. Res.*, *109*, E02009, doi:10.1029/2003JE002179.

Poulet, F., et al. (2009a), Quantitative compositional analysis of Martian mafic regions using the MEx/OMEGA reflectance data: 2. Petrological implications, *Icarus*, *201*, 84–101.

Poulet, F., J.-P. Bibring, Y. Langevin, J. F. Mustard, N. Mangold, M. Vincendon, B. Gondet, P. Pinet, J.-M. Bardintzeff, and B. Platevoet (2009b), Quantitative compositional analysis of Martian mafic regions using MEx/OMEGA reflectance data: 1. Methodology, uncertainties and examples of application, *Icarus*, *201*, 69–83.

Rogers, A. D., and P. R. Christensen (2007), Surface mineralogy of Martian low-albedo regions from MGS-TES data: Implications for upper crustal evolution and surface alteration, *J. Geophys. Res.*, *112*, E01003, doi:10.1029/2006JE002727.

Schaber, G. G., K. L. Tanaka, and J. K. Harmon (1981), Syrtis Major revisited: A highland volcanic planum, not a planitia, paper presented at Third International Colloquium on Mars, *LPI Contrib.*, *441*, p. 223.

Settle, M. (1979), Formation and deposition of volcanic sulfate aerosols on Mars, *J. Geophys. Res.*, *84*, 8343–8354.

Sunshine, J. M., and C. M. Pieters (1993), Estimating modal abundances from modified from spectra of natural and laboratory pyroxene mixtures using the modified Gaussian model, *J. Geophys. Res.*, *98*, 9075–9087, doi:10.1029/93JE00677.

Sunshine, J. M., C. M. Pieters, and S. F. Pratt (1990), Deconvolution of mineral absorption bands: An improved approach, *J. Geophys. Res.*, *95*, 6955–6966, doi:10.1029/JB095iB05p06955.

Tanaka, K. (1986), The stratigraphy of Mars, *J. Geophys. Res.*, *91*, E139–E158, doi:10.1029/JB091iB13p0E139.

B. L. Ehlmann, J. F. Mustard, J. R. Skok, and M. B. Wyatt, Department of Geological Sciences, Brown University, Providence, RI 02912, USA.

S. L. Murchie, John Hopkins University Applied Physics Laboratory, Laurel, MD 20723, USA.